INVESTIGATION OF HYPERVELOCITY MASSIVE PROJECTILE-
GRAPHENE INTERACTION AND CHARACTERIZATION OF INDIVIDUAL
FREE-STANDING NANOPARTICLES IN THE TRANSMISSION DIRECTION
BY MASSIVE CLUSTER SECONDARY ION MASS SPECTROMETRY

A Dissertation

by

SHENG GENG

Submitted to the Office of Graduate and Professional Studies of
Texas A&M University
in partial fulfillment of the requirements for the degree of

DOCTOR OF PHILOSOPHY

Chair of Committee,	Emile Schweikert
Committee Members,	David Russell
	James Batteas
	Jaime Grunlan
Head of Department,	Simon North

May 2017

Major Subject: Chemistry

ABSTRACT

It has been shown that secondary ion emission from ultra-thin foils is notably enhanced in the transmission direction. This feature should be of interest for examining nano-objects. A pre-requisite is to deposit them on as thin a support as possible. For this study graphene was chosen. Free-standing graphene was bombarded alone and with deposition of dispersed nanoparticles in a setup enabling bombardment at $0°$ and secondary ion (SI) detection in transmission in-line with the incident projectiles. $C_{60}^{1,2+}$ and Au_{400}^{4+} at impact energies of ~ 0.4, 0.8 and 1.2 keV/atom respectively were used as primary ions. The experiments were run as a sequence of single projectile impacts with each time separate recording of the SIs identified via ToF-MS.

In order to improve the understanding of the graphene as a potential quasi-immaterial substrate for the deposition of sub-monolayer nanoparticles, the 1-layer and 4-layer graphene were impacted by the individual 25 and 50 keV $C_{60}^{1,2+}$ projectiles and negative SIs and secondary electrons (SEs) were collected in the transmission direction. The yields of C_n^- ($n \leq 4$) are above 10% and decrease exponentially with n. The results are explained with the aid of molecular dynamics (MD) simulation. The ionization probability was estimated by comparing the SI yields of C_n^- to the yields of C_n^0 from MD simulation. The ions come from the thermally excited rim of the impact hole damped by cluster fragmentation and electron detachment. The SE probability distributions are Poisson-like, and on average 3 thermal electrons are emitted per impact. The interaction of a 2D projectile on a 2D target is fundamentally different from that on a 3D material.

1-layer graphene was also impacted by the 440-540 keV Au_{400}^{4+} projectiles in both

positive and negative ion modes in the transmission direction. The projectiles penetrated the graphene and the $Au_{1-3}^{\pm}$ fragment ions were observed as well as $C_n^{\pm}$. During the impact, $\sim15\%$ of the initial kinetic energy is lost. The Au projectiles are neutralized when approaching the graphene, and then partially ionized again (positively and negatively) via electron tunneling from the hot rims of the impact hole on graphene. The projectiles obtain an internal energy of ~500 eV (~4900 K) after the impact. They undergo a ~90 step fragmentation with the ejection of Au_1 atoms in the experimental time range of ~0.1 μs.

Individual free-standing 5 nm gold nanoparticles coated with dodecanethiol were deposited on graphene film and bombarded with Au_{400}^{4+} and $C_{60}^{1,2+}$. The graphene substrate contributed few SIs beyond m/z 120, facilitating the detection of moieties attached to the nanoparticles. Compared to reflection SIMS, transmission SIMS shows a ~4 times higher effective yield of molecular ions from the dodecanethiol coating. The SI yields from Au_{400}^{4+} impact are ~3 times higher than those from C_{60}^{2+} impact. The yield of the dodecanethiol molecular ion is 1.0×10^{-4} from the Au_{400}^{4+} bombardment and 3.0×10^{-5} from the C_{60}^{2+} bombardment. In this case, assuming the Au nanoparticles are perfectly coated by the dodecanethiol molecules, the limit of detection is $\sim5\times10^4$ dodecanethiol molecules with Au_{400}^{4+} bombardment.

ACKNOWLEDGEMENTS

I would like to take this opportunity to thank all of the people who helped me in the past five years in Texas A&M University when pursuing my PhD degree.

Firstly, I would like to thank my advisor, Dr. E. Schweikert. His thoughtful advice and meticulous help always push me forward on the road of graduate study. Without him I'm not sure I would even make it eventually. Thanks to my committee members, Dr. D. Russell, Dr. J. Batteas, Dr. J. Grunlan and Dr. A. Holzenburg, who helped me in my research and coursework. Also, I would like to thank the other instructors of the courses I took here: Dr. S. Wheeler, Dr. D. Son and especially Dr. G. Vigh, who is the most enthusiastic teacher I've ever seen. Thanks to Dr. Y. Bisrat, who taught me how to use the SEM instrument, and Mr. R. Littleton and Dr. H. Kim, who taught me how to use the TEM instrument.

I give special thanks to Dr. S. Verkhoturov, who taught me how to use the C_{60}-SIMS instrument hand by hand, and provided decent results to the models and calculations in my study. Special thanks also go to Dr. C.-K. Liang, who taught me how to use the Au_{400}-SIMS instrument and gave much help to me in the routine work, and to Dr. M. Eller, who coded and continuously updated the data acquisition/analysis software and devoted himself to the improvement of the instruments and the lab environment. Thanks to Dr. F. Yang, Mr. A. Clubb and Mr. D. Verkhoturov, for their help on the instrumentation operation and result discussion, and to Dr. J. DeBord for the technical drawings of the Wien Filter, etc. Thanks to Dr. S. Della-Negra for the fruitful discussions.

I would like to thank all of the members in the Center for Chemical Characteri-

CONTRIBUTORS AND FUNDING SOURCES

NOMENCLATURE

AuNP   Gold nanoparticles

CFD   Constant fractional discriminator

CMOS   Complementary Metal-Oxide-Semiconductor

CVD   Chemical Vapor Deposition

EEM   Electron emission microscope

IPNO   Institut de Physique Nucléaire d'Orsay

LMIS   Liquid metal ion source

LoD   Limit of detection

MCP   Microchannel plate

MD   Molecular dynamics

MS   Mass spectrometry

NP   Nanoparticle

PI   Primary ion

SE   Secondary electron

SEM   Scanning electron microscope

SAMPI   Surface Analysis and Mapping of Projectile Impacts

SI   Secondary ion

SIMS   Secondary ion mass spectrometry

TEM   Transmission electron microscope

TME   Total Matrix of Events

TDC   Time-to-digital converter

ToF   Time of flight

TABLE OF CONTENTS

LIST OF TABLES

1. INTRODUCTION

The rationale for examining individual nanoparticles is to enable a more nuanced understanding of their functionalities.[1, 2] The most pronounced changes in chemical reactivity are expected to occur when they are of smallest size.[3] Yet when surface-to-volume ratios are large, heterogeneity becomes a major concern. Thus to maximize accuracy, assays should be on individual nanoparticles rather than an ensemble of nanoparticles. However extracting chemical information from a single vanishingly small object is very difficult to impossible. The limitation can be side-stepped by probing a large number of dispersed nanoparticles one-by-one and recording the emissions from each nanoparticle separately. A large collection of nanoparticles will likely contain subsets of like-nanoparticles. Their data can be summed for statistics.[4]

The prerequisite for the above approach is an analysis technique which can extract information from individual nanoparticles. SIMS with massive clusters as projectiles has been shown to provide exquisite detection sensitivity.[5, 6] The projectiles of choice in this study are $C_{60}^{1;2+}$ and Au_{400}^{4+}. At impact energies of ~1 keV/atom, they generate high ion multiplicities. For instance, Van Stipdonk et al.[5] reported a 5-80 times enhancement of the molecular ion yield from the phenylalanine target using C_{60}^{+} as projectiles compared to the Cs^{+} and Ga^{+} with the same energy. DeBord et al. reported a > 100 times enhancement of the SIs per impact from the Au_{400}^{4+} impact compared to that from the Au_{3}^{+} impact on peptide targets.[6]

The present study focuses on the methodology for characterizing ultrasmall nanoparticles (≤10 nm in diameter). In this size range, the nanoparticle volume is smaller than the volume of the collision cascade induced by the incident ion (~10^3 nm^3)[7] and the SI emission is facilitated by a large surface area. These parameters en-

1

able bombardment-detection in the transmission mode which has been shown earlier, results in increased SI yields.[7, 8, 9] In this approach the support on which the nanoparticles are anchored should ideally be immaterial. Graphene as a single layer or in a few layers was chosen for this purpose. In the absence of any literature, the research had first to address the fundamentals of the projectile-graphene interaction before considering the case of nanoparticles on free-standing graphene.

The impact of one projectile on an ultrasmall nano-object results in complete volatilization. The detection of the SIs and data processing must be designed accordingly. The experiments were run in the "event-by-event bombardment/detection mode". In this mode each impact event was recorded individually so that in a single event SIs are co-emitted and co-localized in the same nanovolume ($\sim 10^3$ nm^3). The SIs were collected in the transmission direction because the SI yield is about one order of magnitude higher[9] compared to that in the conventional reflection direction when an ultrathin target such as graphene is applied.

The present study focuses on three topics: a) fundamentals of hypervelocity C$_{60}$-graphene interaction: SI and SE emissions (Chapter 4); b) fundamentals of Au$_{400}$-graphene interaction: SI emission and projectile fragmentation (Chapter 5); and c) characterization of individual free-standing nanoparticles on graphene in transmission (Chapter 6).

The first topic includes the first experimental data of C$_{60}^{1,2+}$ (25 keV and 50 keV) impact on 1-layer and 4-layer free-standing graphene target. The goal here was to gain insight into the mechanism of the emission of secondary ions and electrons from the confined volume of the 2D material in the transmission direction using both the experimental data and the MD simulation.

The second topic concerns the study of hypervelocity Au$_{400}^{4+}$ (440-540 keV) impact on 1-layer free-standing graphene target. Except for the C$_n^{\pm}$ SIs coming from the

graphene, $Au_{1-3}^{\pm}$ and the projectiles that penetrate the graphene were also observed in the transmission direction. The goal of this study was not only the investigation of the SI emission, but also to establish the energy balance (kinetic energy, internal energy, and energy loss) of the projectile during the impact, and the fate of the projectile after the impact.

The third topic deals with the characterization of sub-monolayer free-standing 5 nm dodecanethiol-coated gold nanoaparticles deposited on the 4-layer graphene with massive cluster projectile ($C_{60}^{1,2+}$ and Au_{400}^{4+}) impact. The SIs were also collected in the transmission direction. The goal was to investigate the projectile-dependent SI emission of the molecular ions, and to evaluate the SI yields in the transmission direction versus in the reflection direction.

The account of these investigations is proceeded by a brief literature summary on SIMS, of the concept of coincidence measurements and on the analysis of individual nanoparticles (Chapter 2), followed by a description of the instrumentation, data analysis and sample preparation (Chapter 3).

2.   LITERATURE REVIEW

2.1   Secondary ion mass spectrometry

Secondary ion mass spectrometry is based on bombarding a solid surface with the projectiles (primary ions) of keV to MeV energy. The energy transferred by the incident projectiles cause a collision cascade that sets surface atom layers in motion concurrent with complex process of energy transfer in the surface region. The result is the emission of electrons, photons, atoms, molecular fragments and molecules. A small fraction (typically 0.01%) of the atoms, molecular fragments and molecules are ionized. These secondary ions are identified by the mass spectrometer.

SIMS is a surface analysis technique. Each projectile probes a small volume of the sample surface and provides the chemical characterization (see the discussion below) Like other MS techniques, SIMS is intrinsically useful to obtain molecular information from the analytes.

2.2   Static SIMS

If the impact rate of the projectiles is less than 10^{12} ions/cm^2, it is unlikely that the same spot of the sample surface is impacted by the projectiles twice.[10] In other words, each projectile probes an intact area of the surface, and most surface area is not destroyed in the experiment. This is known as static SIMS. In this mode, fragmentation of the molecular ions of the analyte is reduced, facilitating the detection of analyte-specific ions. In order to improve the low SI signals due to the limited primary ion dose, cluster projectiles were introduced. They can increase the efficiency of the SI emission, especially for molecular fragments and molecular ions.

4

2.3   Cluster projectiles

In conventional SIMS, the primary ions are usually atomic ions (Ga^+, Cs^+, O_2^+, etc.[11]) with keV kinetic energies. In the late 1980s, several investigators showed that cluster ions generate large enhancement in SI yields. (The yield is defined as the number of detected SIs per impact. See the discussion in Chapter 3.) In 1989, Appelhans et al.[12] observed a 10-25 times of enhancement of the molecular ion yield when bombarding the organic surface with SF_6^0 and SF_6^- compared to the Cs^+ projectile with similar energy and mass. In the same year Blain et al.[13] observed that the SI yield is directly proportional to the momentum of the projectile when using $(CsI)_nCs^+$ projectiles. The "cluster effect" is attributed to overlapping collision cascades due to the coherence in the bombardment by polyatomic ions. The non-linear enhancement in SI yields for cluster projectiles versus atomic projectiles at equal velocity has been observed for clusters with up to 9 constituents.[14] For larger clusters, the enhancement increases linearly with the number of cluster atoms.

The trend of increasing SI with increasing cluster size holds for still larger projectiles as demonstrated in 1996 by Van Stipdonk et al.[5] with the introduction of a C_{60} source. They showed that C_{60}^+ at the same energy as Cs^+ or Ga^+ produced 5 to 80 times higher SI yields. C_{60} has now become a routine beam in SIMS instruments.[15] More recently, Tempez et al. showed that still larger SI yields could be obtained with Au_{400}^{4+}.[16] A 1000-fold increase in SI yields was reported for Au_{400}^{4+} over Au^+ at the same energy per charge. The advantageous characteristics of Au_{400}^{4+} were confirmed by DeBord et al. who observed $\sim$100 SIs per impact of one Au_{400}^{4+} versus 0.76 SI per impact of Au_3^+ at 50 keV on 4 peptide targets.[6]

2.4 Transmission SIMS

The first observation of enhanced SI emission in the transmission direction was reported by DeBord et al. with 5-20 nm carbon foils.[7]. The same trend was confirmed with an ultra-thin substrate such as graphene.[9, 17] Graphene as a quasi-immaterial substrate for analytes maximizes the limit of detection. Compared to a bulk substrate, SIs emitted from graphene are about one order of magnitude less than those from the bulk substrate due to the thickness of graphene (0.34 nm, graphite interlayer spacing[18]). As a consequence a sub-monolayer of nanoparticles deposited on graphene substrate can be detected under optimal conditions in the transmission direction. Moreover, graphene is robust enough to support nanoparticles.[19, 20], and oxidized/functionalized graphene with a variety of functional groups facilitates the anchoring of nanoparticles. In the previous studies, Liang et al.[17] reported that SI emitted from ultra-small (5 nm) gold nanoparticles could be distinguished from the 1-6 layer graphene substrate. Eller et al.[9] studied the hypervelocity Au_{400}^{4+} impacts on free-standing graphene, and reported that the observed SI yields of carbon clusters in the transmission direction were 10-15 times higher than those in the reflection direction. Surprisingly the SI emission was largely independent of the thickness, suggesting that the emission of SIs is a surface phenomenon. The size of the holes on few-layer graphene produced by projectiles are 8.3-9.2 nm in diameter, which is much larger than the $\sim$2 nm Au_{400}^{4+} projectiles.

The above observations indicate that the interaction between the hypervelocity massive cluster and a 2D material is fundamentally different from that with a 3D material. The confined volume of 2D materials lacks sufficient dimensions for complete energy deposition, indicating that a different mechanisms operate for ejection-ionization of the secondary ions. The secondary ions can be collected in

both reflection and transmission direction when the target is a 2D material, and the latter provides higher secondary ion yields. In the transmission direction, the intact projectiles and the fragments are also collected, which provides another tool for the study of the cluster-2D material interaction, and the fate of the projectiles after the interaction.

2.5   Coincidence measurements

As noted earlier when an individual nanoparticle or a nanodomain is bombarded with a single massive cluster at impact energies of $\sim$1 keV per atom, they generate emission of multiple secondary ions. Thus it becomes feasible to record the secondary ions from each impact individually. In a single impact event, SIs are co-emitted, therefore co-localized from the same nanovolume.[4] Each event corresponds to the chemical composition of the nanovolume probed by one cluster impact, i.e., an area of 10-15 nm in diameter and up to 10 nm in depth.[7] In other words, the data from the individual nanovolume can be selected to show for example a specific secondary ion, which in turn will reveal the co-emitted secondary ions. This method is referred to as the "event-by-event bombardment/detection mode".[4] In this mode, the impact events are resolved in space, making it feasible to map the distribution of an ion of interest. Eller et al. reported first the real-time localization of single C_{60} impacts via the ejected SEs with correlated SI detection[21] and the methodology for mapping of co-localized organic samples[22].

In practice, the success of this approach depends on suitable sample preparation technique and the instruments designed to maximize the detection of secondary ions. The event-by-event bombardment/detection mode and the coincidental ion mass spectrum are further discussed in Chapter 3.

2.6 Analysis of individual nanoparticles

Most of the previous work of the individual nanoparticle characterization has been based on laser desorption/ionization (LDI). In 1973, the first MS of individual particles was reported by Davis et al.[23] Particles of inorganic salts (e.g. $SrCO_3$ and CuO) on a metal surface were heated and vaporized. The measurement of individual nanoparticles suspended in air became practical in 1991 when McKeown et al.[24] combined the LDI to time-of-flight (ToF) mass spectrometer. In 2003, the first rapid single particle mass spectrometer (RSMS) was developed by Lake et al.,[25] which was able to make online single particle measurements of ambient ultrafine aerosol (down to 30 nm in aerodynamic diameter). Further developments led to ultrafine aerosol time-of-flight mass spectrometry (UF-ATOFMS) in 2004.[26, 27] Nano aerosol mass spectrometry (NAMS) was developed by Wang et al. in 2006.[28, 29] In MANS, nanoparticles are sized by electrodynamics rather than aerodynamics. NAMS is capable of single nanoparticle analysis in the 10-30 nm range.

The application of SIMS on individual nanoparticles has been studied in the Schweikert lab since 2008 with the following results. Size-dependent SI emission of individual Al_2O_3 nanoparticles obtained from the Au_{400} SIMS was reported by Pinnick et al.,[30] where SI mass shifted to low-mass area when the size of the isolated nanowhiskers ($\sim$2 nm in diameter and $\sim$200 nm in length) were below the size of the desorption volume (estimated $\sim$10^3 nm^3), and the relative abundance of AlO^- and AlO_2^- from the whiskers and from the bulk sample were different. Rajagopalachary et al.[31] reported that the single or multilayer organization of individual 5 nm silver nanoparticles were tested and the surface coverage were determined. Chen et al.[32] reported that the number of antibody-AuNP conjugates on the surface of a cell was measured by SIMS as $\sim$42000 per cell, which is in good agreement with literature

results. Eller et al.[33] reported that the SE emissions are dependent on the size and surroundings of the nanoparticles, but independent of the SI emissions with different surface topography and size. Liang et al.[34] showed that projectile-dependent and size-dependent SI emission from 2-50 nm gold nanoparticles, and provided the first quantitative measurements of SI yields.

3. INSTRUMENTATION AND METHODOLOGY

3.1 C_{60} effusion source

The experiments in Chapter 4 and 6 were performed with a custom-built SIMS instrument equipped with a C_{60} effusion source.[33, 35] In this source, the C_{60} powder (Sigma-Aldrich, St. Louis, MO) is placed in a copper reservoir and heated to above its sublimation temperature ($\sim 450\,°C$). In front of the reservoir is a tantalum disc which is heated to emit electrons that are accelerated to 85 eV. After the C_{60} molecules leave the reservoir through a nozzle they are struck by the accelerated electrons and ionized to C_{60}^{q+} ($q = 1, 2, 3$) primary ions. The temperature of the Ta disc regulates the rate of electrons emitted, which determines the rate of C_{60}^{q+} ions generated. The ions are then extracted and accelerated up to $15q$ keV. After the acceleration the ions pass through two pairs of deflector plates and leave the source chamber (Figure 3.1). Next they enter a Wien filter, which is a mass analyzer with orthogonal electric and magnetic fields designed to separate ions with different velocities (see the discussion below). The projectiles selected by the Wien filter pass through a 200 μm pinhole, another two pairs of deflector plates, and an Einzel lens. Finally the projectiles are further accelerated to $25q$ keV by the -10 kV biased target and impact on it at an incident angle of $0°$ on a focused area of less than 200 μm in diameter with a rate of 1000-2000 impacts per second, which is appropriate for the "event-by-event bombardment/detection mode" (see the discussion below).

The impacts of C_{60} projectiles on the sample generate electrons, ions, and neutrals. The electrons and negative ions are extracted from the nanodomain on the target and accelerated to 10 keV in the transmission direction. After being focused and directed by a lens and two pairs of deflector plates, the SIs and SEs are sepa-
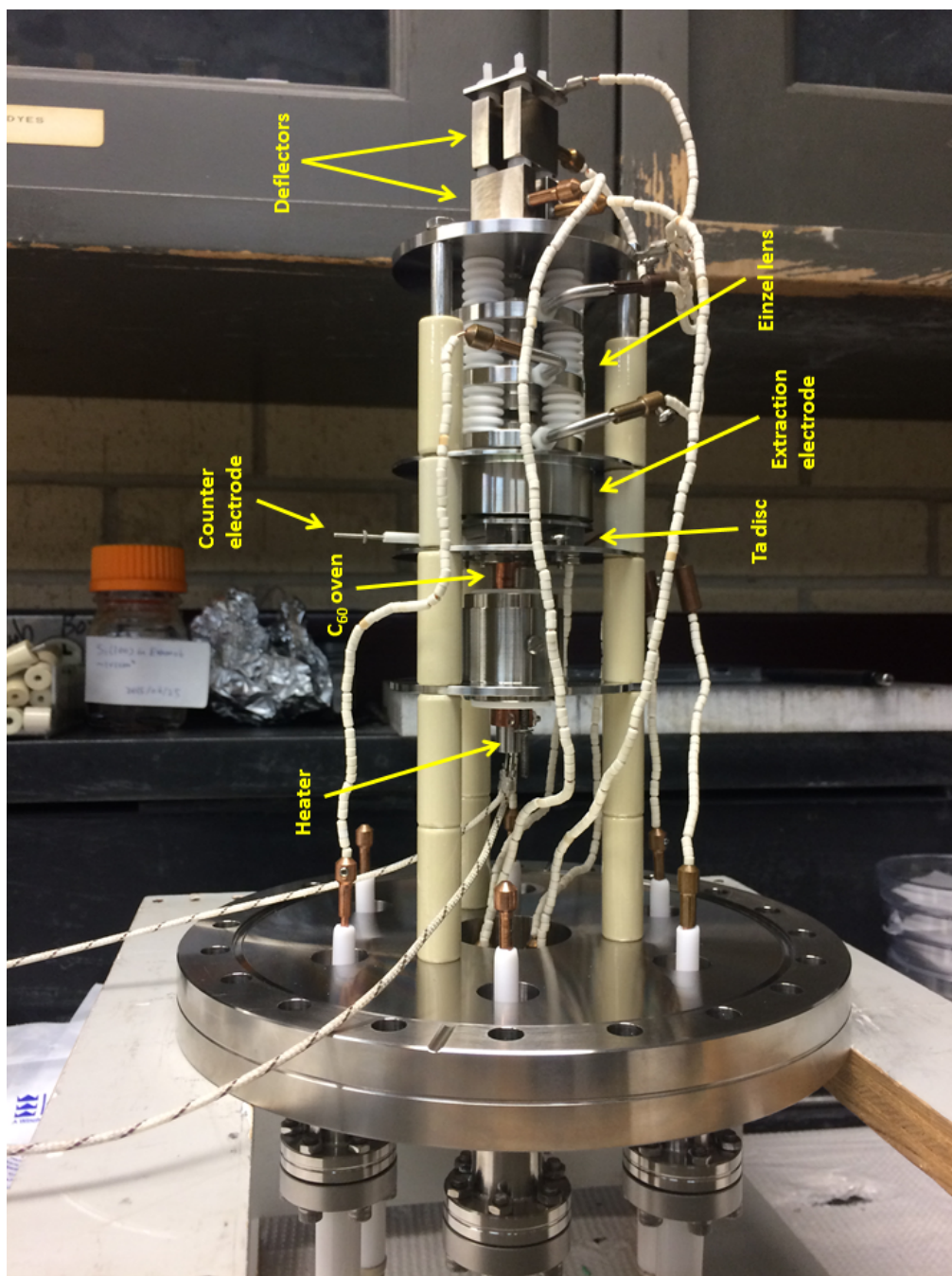
Figure 3.1: Picture of the C_{60} effusion source.

rated using an electromagnet with a weak magnetic field ($\sim$100 gauss). The SEs are focused and deflected to the start detector through the electron emission microscope (EEM) with 4 additional lens and deflector pairs.[35, 22] The detectors is discussed below. At the same time, the SIs generated from the target follow a straight path into the 1.2 m linear ToF mass spectrometer (unaffected by the weak magnetic field due to their much heavier masses in comparison to electrons), and are focused on the 8-anode stop detector . The schematic setup of the C_{60}-SIMS instrument is shown in Figure 3.2. A picture of this instrument is shown in Figure 3.3.

The primary ions generated and accelerated from the same source carry the same amount of kinetic energy, E_k, which can be calculated as follows:

$$qU_S = E_k = \frac{1}{2}mv_S^2 \tag{3.1}$$

therefore,

$$v_S = \sqrt{\frac{2qU_S}{m}} \tag{3.2}$$

where q is the charge of the projectile, U_S is the source acceleration voltage, E_k is the kinetic energy of the projectile obtained, m is the mass of the projectile; and v_S is the velocity of the projectile when leaving the source.

Considering that the projectile is accelerated when approaching the biased target, Eq. 3.1 can be modified to:

$$q(U_S - U_T) = E_k' = \frac{1}{2}mv_T^2 \tag{3.3}$$

therefore,
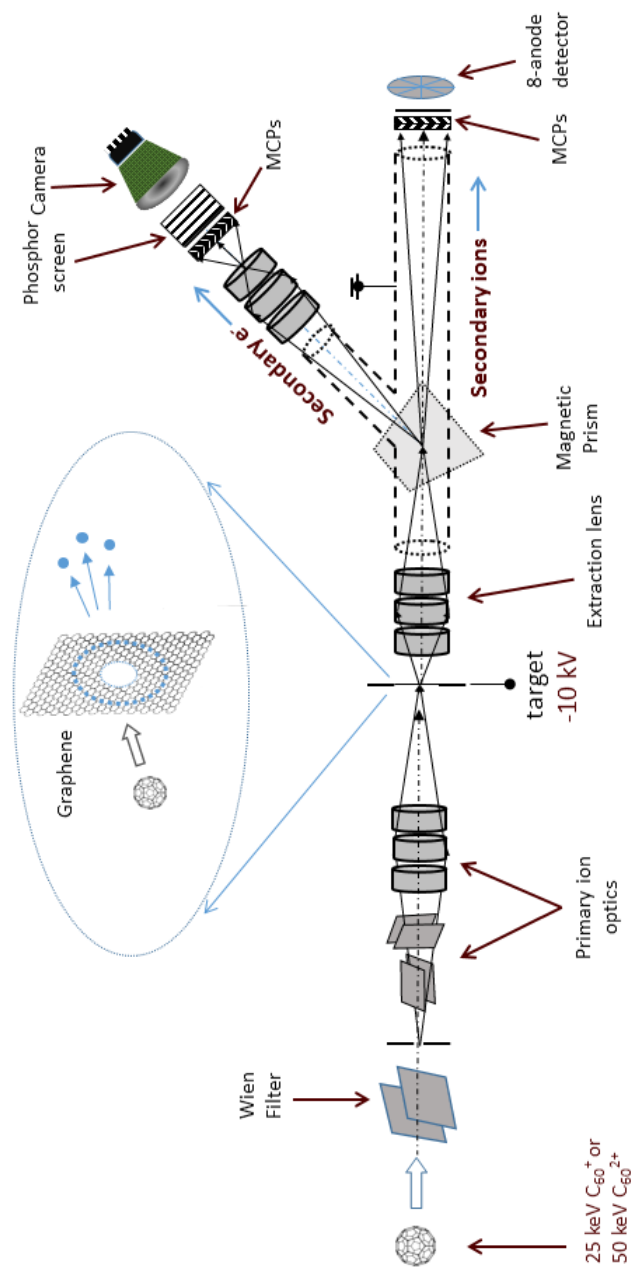
Figure 3.2: Schematic setup of the C_{60}-SIMS instrument.
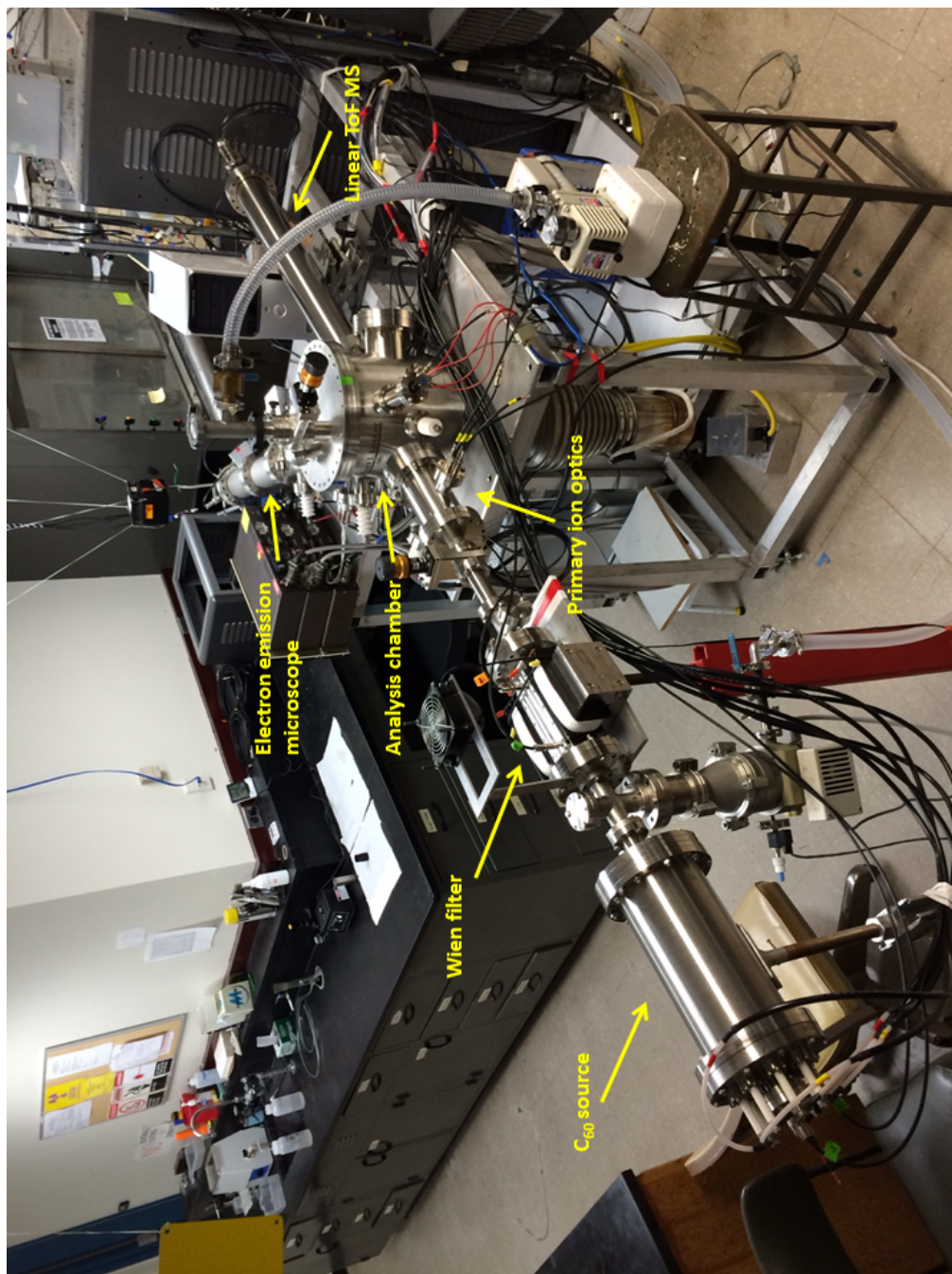
Figure 3.3: Picture of the C_{60}-SIMS instrument.

$$v_{\mathrm{T}} = \sqrt{\frac{2q(U_{\mathrm{S}} - U_{\mathrm{T}})}{m}} \tag{3.4}$$

where U_{T} is the voltage applied to the target, and v_{T} is the velocity of the projectile when impacting the target. For 25 keV C_{60}^+ and 50 keV C_{60}^{2+} projectiles, the corresponding impact velocities are 82 km/s and 116 km/s according to Eq. 3.4.

3.2 Au liquid metal ion source

The experiments in Chapter 5 and 6 were performed with another custom-built SIMS instrument with a Au liquid metal ion source (Au-LMIS). The whole source assembly, including the Wien fitler, is built on the Pegase high voltage platform, designed and built at the IPNO, Orsay, France.[8, 36] In this source, the Au-Si eutectic (97%-3%, Academy Precision Metals, Albuquerque, NM) is used to reduce the melting point of Au from 1064 °C to ∼360 °C. The eutectic is placed in a spring-like reservoir made of tungsten wire (ϕ 0.200 mm, Alfa Aesar, Tewksbury, MA) with a tungsten needle through it made by a ϕ 0.200 mm tungsten wire with an electro-chemically etched tip. The reservoir is heated to above ∼ 360 °C, the molten Au moves towards the tip of the needle and is extracted by the 6-10 kV biased electrode with a hole in front of the tip (< 1 mm off). When the Au droplets leave the tip, a Taylor cone is formed between the needle tip and the extraction electrode. The source part is floated to 20 kV relative to the high voltage platform.

A large variety of Au projectiles, including Au_{1-9}^+ and a large distribution extending from m/z 2000 to m/z 30000,[8] are generated from the Au-LMIS source. The distribution of n/q of Au projectiles is regulated by the extraction current. A Wien filter is used to select the ion with a specific n/q value (in the experiments performed, Au_{100q}^{q+} ions were selected at an extraction current of 50 μA with a most probable q of 4[37]). A Faraday cup in front of the Wien filter is used to measure

the current of the total beam or the selected ion. Typically, A total beam of ~200 nA and a beam of Au_{400}^{4+} of ~400 pA can be obtained. When the Faraday cup is retracted, the selected Au ions can leave the high voltage platform (100 kV floated) with a kinetic energy of $120q$ keV (for Au_{400}^{4+}, the kinetic energy is 480 keV). The projectiles are deflected by 3 pairs of deflectors between the platform exit and the target in the 1st analysis chamber. Two collimators are used here. The 1st collimator is between the 1st and 2nd deflector pairs with 0.5 mm and 1 mm slits. and the 2nd collimator is just in front of the target with ϕ 0.25 mm, ϕ 0.5 mm and ϕ 5 mm holes. A pulser (±1000 V) is used to decrease the impact rate to make sure that it is unlikely 2 projectiles impact the sample at the same time. The pulser also provides ToF start signals for the positive ion mode. The typical pulsing rate is 3-10 Hz. The 1st analysis chamber includes a reflectron ToF-MS with an EEM for SE detection. The detailed description of the 1st analysis chamber can be found elsewhere[8]. In this dissertation the MS in the 1st analysis chamber is not used.

In the transmission SIMS experiments (Chapter 4, 5 and 6), the target is in the 2nd analysis chamber. When the target in the 1st analysis chamber is retracted, the projectiles are further steered and focused on the target by the deflectors and Einzel lens between the 1st and 2nd analysis chamber. The target is usually -10 kV or +10 kV biased in the negative or positive modes. The Au_{400}^{4+} projectiles impact on it at an incident angle of 0° with a rate of ~1000 impacts per second (at 3-10 Hz of the pulsing rate), which is appropriate for the "event-by-event bombardment/detection mode" (see the discussion below). The impact area on the sample is 2-3 mm in diameter. The impacts of Au_{400}^{4+} projectiles on the sample generate SEs and SIs. All charged species, including the projectiles (intact/fragmented) penetrating through the target, are accelerated to 10 keV in the transmission direction (when the target bias is -10 kV or +10 kV). The SIs and SEs are separated using an electromagnet. The SEs

16

are deflected to the start detector directly. At the same time, the projectiles and SIs fly through a 66 cm linear ToF mass spectrometer and reach the 16-anode stop detector. The detectors are discussed below. The schematic setup of the Au_{400}-SIMS instrument is shown in Figure 3.4.

3.3 Wien filter

A Wien filter is a device to seperate charged particles with orthogonal electric field and magnetic field. The charged particles travelling through a Wien filter experience the Lorentz force, which is the combination of the electric force and magnetic force:

$$\vec{F_{L}} = q\vec{E} + q\vec{v} \times \vec{B} \tag{3.5}$$

where $\vec{F_{L}}$ is the Lorentz force, q is the charge of the particle, $\vec{v}$ is the velocity of the particle, $\vec{E}$ is the electric field and $\vec{B}$ is the magnetic field. In the Wien filter, only the charged particles experiencing zero Lorentz force pass straight. The other particles are steered:

$$q\vec{E} + q\vec{v} \times \vec{B} = 0 \tag{3.6}$$

Because the electric field and the magnetic field are orthogonal in the Wien filter, Eq. 3.6 can be simplified to:

$$qE = qvB \tag{3.7}$$

thus,

$$v = \frac{E}{B} \tag{3.8}$$

17
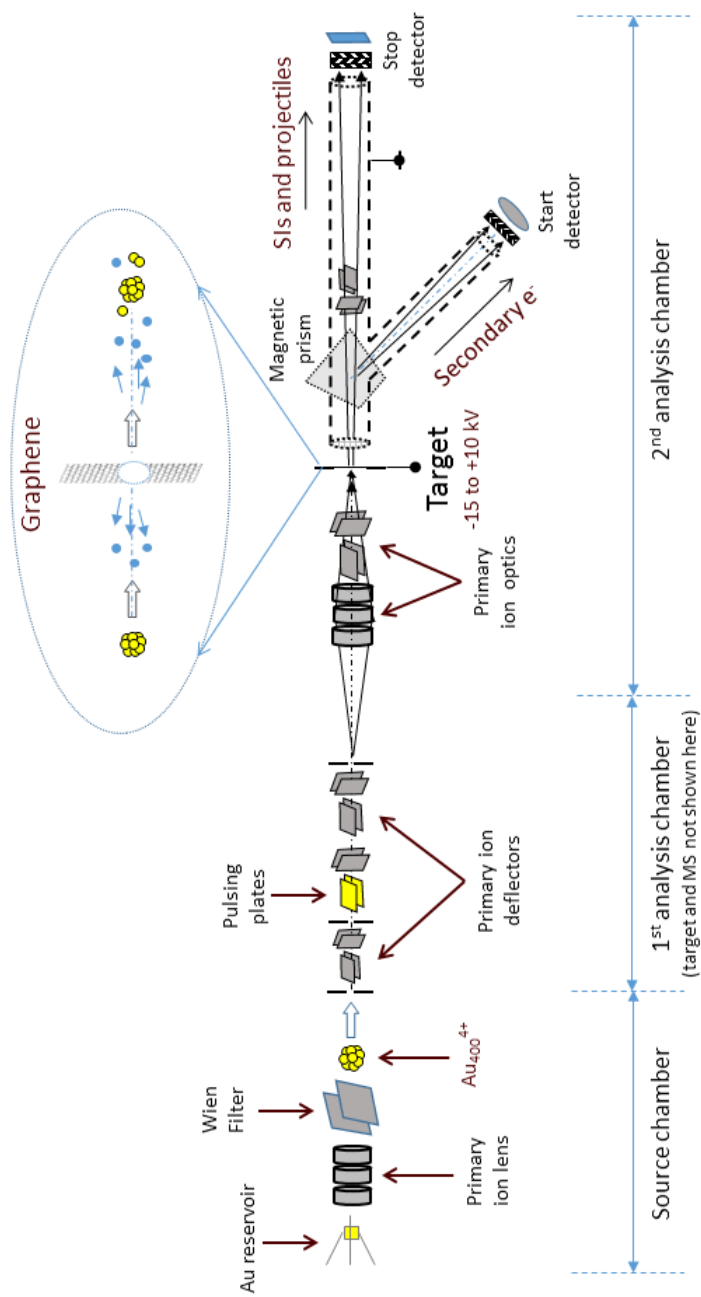
Figure 3.4: Schematic diagram of the Au_{400}^{4+} SIMS instrument.

Eq. 3.8 indicates that a Wien filter is essentially a velocity selector. According to Eq. 3.2, we have $v \propto (q/m)^{1/2}$. Therefore a Wien filter can select a set of projectiles with the same mass-to-charge ratio (if they are generated from the same source). In our experiments, $C_{60}^{1,2+}$ (Figure 3.5) and Au_{400}^{4+} (Figure 3.6) are selected out using the Wien filter.

3.4   Time-of-flight mass analyzer

In all of the experiments run in the C_{60} and Au_{400} SIMS instruments, described in Chapter 4-6, linear time-of-flight (ToF) mass analyzers were used. The ToF mass analyzer resolves ions by the difference of their flight time. In a ToF-SIMS, an ion emitted from the target flies through an acceleration region, a field-free region, and a deacceleration region before it reaches the detector (Figure 3.7).

The total flight of an ion is determined by the summation of the flight times in those three regions:

$$t_{\mathrm{F}} = t_{\mathrm{ac}} + t_{\mathrm{ff}} + t_{\mathrm{de}} \tag{3.9}$$

where t_{F} is the total flight time, t_{ac} is the flight time in the acceleration region, t_{ff} is the flight time in the field-free region, and t_{de} is the flight time in the deacceleration region. These flight times can be calculated as follows:

$$t_{\mathrm{ac}} = \sqrt{\frac{2d_{\mathrm{ac}}^2 m}{qU_{\mathrm{T}}}} \tag{3.10}$$

where d_{ac} is the distance between the target and the first grounded grid, which is also the length of the acceleration region, m is the mass of the SI, q is the charge of the SI, and U_{T} is the voltage applied on the target.
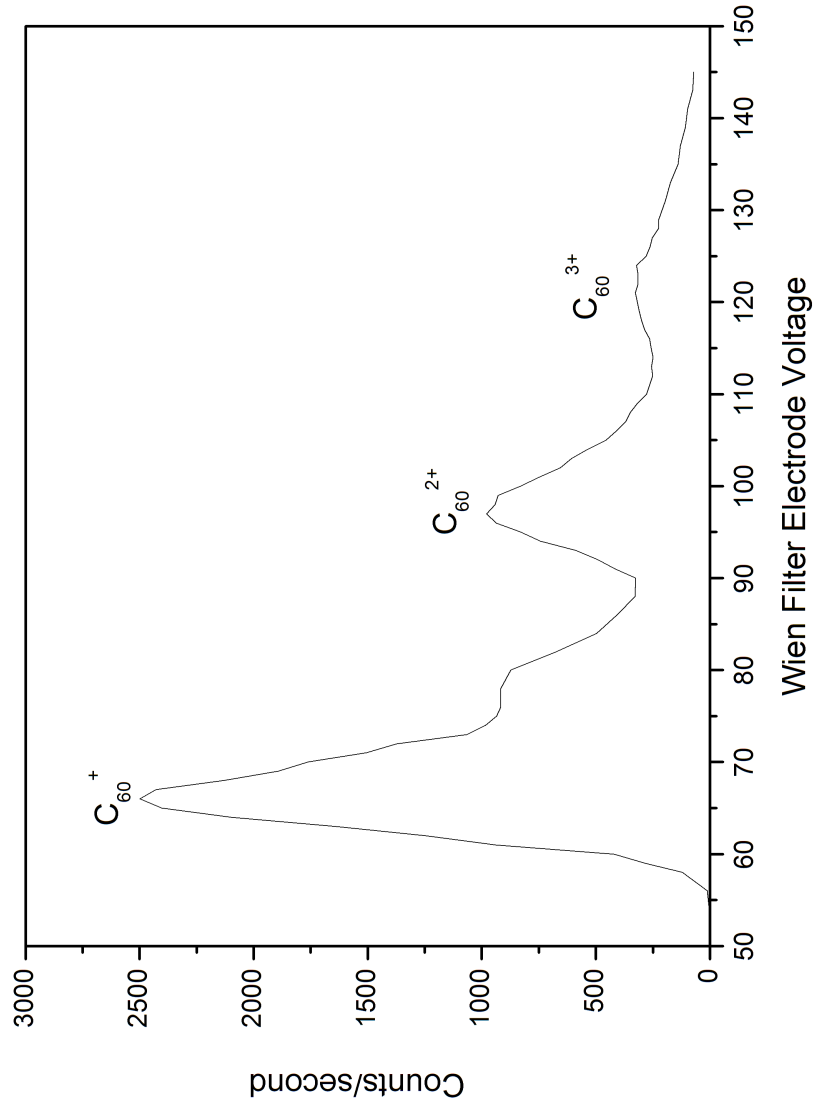
Figure 3.5: Wien Filter selection of the C_{60}^{q+} primary ions. C_{60}^{1+}, C_{60}^{2+} and C_{60}^{3+} are clearly separated.
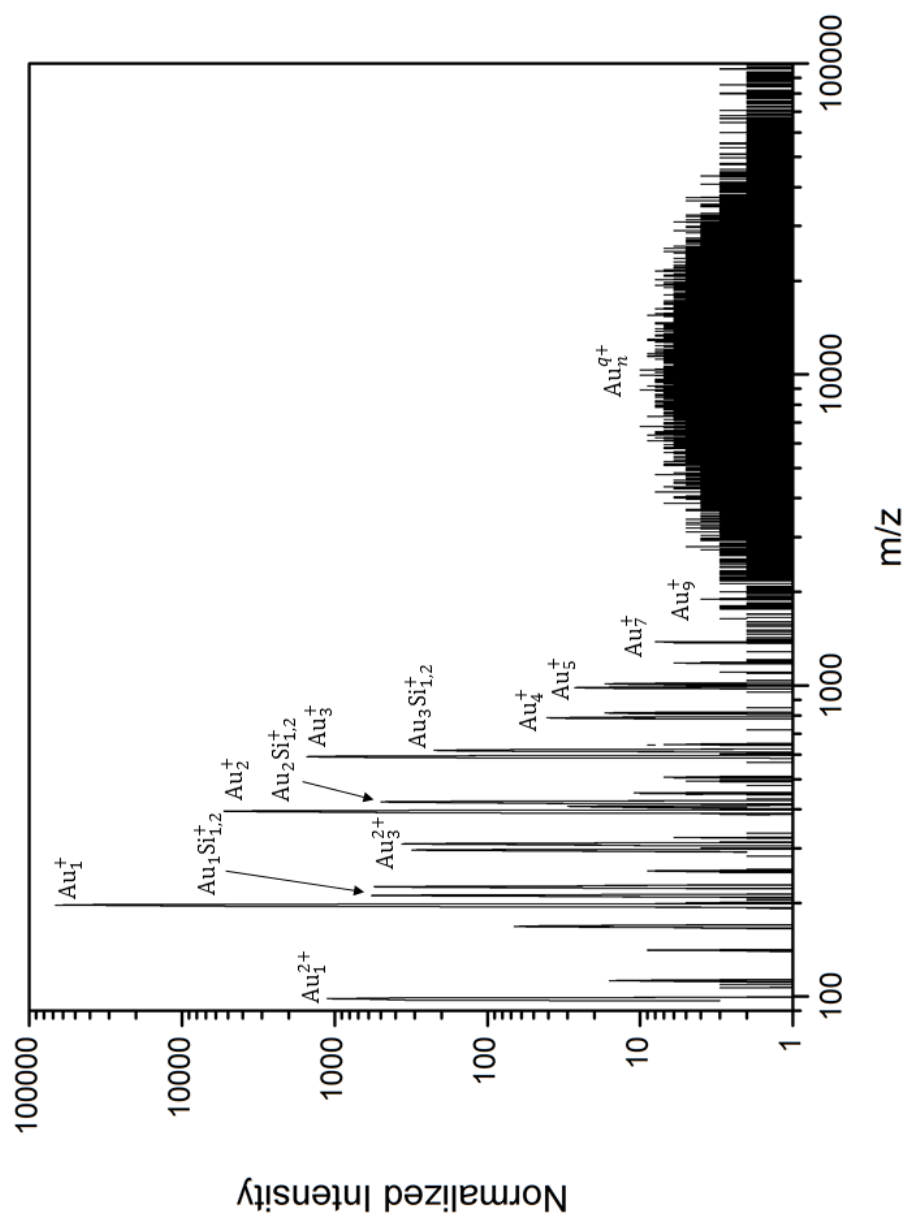
Figure 3.6: Wien Filter selection of the Au clusters emitted from the Au-LMIS (i.e. the primary ion mass spectrum).
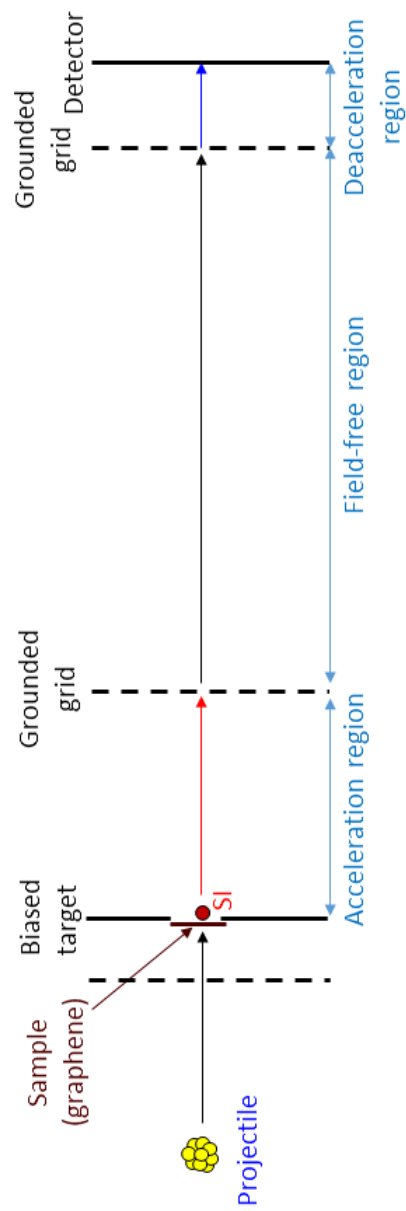
Figure 3.7: Schematic diagram of a linear ToF-SIMS (SIs are emitted in the transmission direction, not drawn to scale).

$$t_{\text{ff}} = \sqrt{\frac{d_{\text{ff}}^2 m}{2qU_{\text{T}}}} \tag{3.11}$$

where d_{ff} is the length of the field-free region.

$$t_{\text{de}} = \sqrt{\frac{2d_{\text{de}}^2 m}{qU_{\text{D}}^2}}(\sqrt{U_{\text{T}} + U_{\text{D}}} - \sqrt{U_{\text{T}}}) \tag{3.12}$$

where d_{de} is the distance between the front plate of the detector and the last grounded grid, which is also the length of the deacceleration region, U_{D} is the voltage applied on the front plate of the detector.

According to Eqs. 3.9 - 3.12, we have:

$$t_{\text{F}} = \sqrt{\frac{m}{q}} \left[\sqrt{\frac{2d_{\text{ac}}^2}{U_{\text{T}}}} + \sqrt{\frac{d_{\text{ff}}^2}{2U_{\text{T}}}} + \sqrt{\frac{2d_{\text{de}}^2}{U_{\text{D}}^2}}(\sqrt{U_{\text{T}} + U_{\text{D}}} - \sqrt{U_{\text{T}}}) \right] \tag{3.13}$$

In the secondary ion mass spectra obtained from our SIMS instruments, most of the SIs are singly charged, i.e. $q = \pm e$. If other conditions are kept constant, Eq. 3.13 can be simplified to:

$$t_{\text{F}} = k\sqrt{m} \tag{3.14}$$

which means in a ToF-SIMS, the flight time of an ion is directly proportional to the square root of its mass.

3.5   Data acquisition system

In the C_{60}-SIMS instrument (Figures 3.2 and 3.3), the SEs were collected on +1.9 kV biased dual microchannel plates (MCPs[38], Photonis, Sturbridge, MA) assembled in a chevron configuration followed by a +2.6 kV biased 50 nm Al-coated phosphor screen and a fast CMOS camera (IDT M3, Tallahassee, FL). The negative voltage

signals on the phosphor screen were transferred to a constant fraction discriminator (CFD, Tennelec TC 454, Oak Ridge, TN), converted to logical ToF start signals and then transferred to an 8-port time-to-digital converter (TDC, CTNM4, IPNO, Orsay, France). Meanwhile, the SIs were collected on -2.3 kV biased dual MCPs with an 8-anode detector. This round-shaped 8-anode detector has an 8 pie-shaped center-symmetric design. The negative voltage spikes on the anode were transferred to a CFD (Ortec CF 8000, Oak Ridge, TN), generating ToF stop signals. The stop signals were transferred to the same TDC mentioned before and processed as time-related events. This stop signals were assigned to different "channels" according to their arrival time relative to the start signal. the width of each channel is 120 ps. Then the acquired data (.tme files, Total Matrix of Events[39]) were processed by SAMPI software, which is discussed below. A 16-port TDC (IPNO, Orsay, France) with a channel width of 120 ps was also used (.edf files were created with this TDC).

The Au_{400}-SIMS instrument had a similar setup (Figure 3.4). The start and stop detectors in the 1st analysis chamber were similar to the ones on the C_{60}-SIMS instrument. The start detector in the second chamber was simple: instead of the phosphor screen, a copper plate was used as the anode of the detector. The bias on the detector was -2.3 kV. The stop signals were collected by triple MCPs with a 16-anode detector (4×4 square-shaped) and the bias on the stop detector was -2.4 kV. A linear discriminator (instead of a CFD) and a 16-port 120-ps TDC were used. The acquired data (.edf files) were processed by SAMPI.[40]

3.6 Data analysis software

Surface Analysis and Mapping of Projectile Impacts, SAMPI©, is a custom-built software for mass spectrum analysis in our lab, programmed by Eller.[40] The .tme and .edf files can be input and the calibrated mass spectra files can be output for

further process by other software (Excel, Origin, etc). The mass calibration can convert a spectrum in time scale to a spectrum in mass scale. According to Eq. 3.14, the relationship between the channel numnber (ch) and the mass of an ion is as follows:

$$ch = a\sqrt{m} + b \qquad (3.15)$$

where a and b are coefficient and are obtained (in SAMPI) by taking a linear regression of 4 known ions in a mass spectrum.

In addition to the normal (total) mass spectrum, it has the ability to generate different kinds of coincidence mass spectra (see the discussion below), secondary ion multiplicity report (see the discussion below), the anode distribution of the total mass spectrum or a selected ion, lists of SI yields, and other useful features.

3.7 Event-by-event bombardment/detection mode

In the "super-static regime" of SIMS, the impact dose is $\leq 10^6$ impacts/cm^2 across the whole experimental time range. At this dose, it is unlikely that two projectiles impact the same spots, thus most SIs come from the pristine sample surface. These impact events can be recorded individually, including the SI information from each impact.[4] This is called "event-by-event bombardment/detection mode". This is important especially when massive clusters ($C_{60}^{1,2+}$ or Au_{400}^{4+}) are used, because they are efficient enough to produce >10 SIs in one event. It is also possible that more than one identical ions are detected simultaneously in one event (by different anodes):

$$Y_A = \sum_{x_A} \frac{x_A N(x_A)}{N_0} = \sum_{x_A} x_A P(x_A) = \frac{I_A}{N_0} \qquad (3.16)$$

where Y_A is the yield of the ion A, x_A is the number of detected A ions in an individual

25

impact (for an n-anode detector, $0 \leqslant x_A \leqslant n$), $N(x_A)$ is the number of events where there are x_A of A ions detected ($N(x_A)$ obeys the Poisson distribution), $P(x_A)$ is the probability distribution of x_A of A ions detected per individual impact, I_A is the total intensity of the ion A, and N_0 is the number of total impacts.

By using SAMPI software, it is possible to obtain the distribution of the number of SIs detected per event (the SI multiplicity) for both the total mass spectrum, and the selected ion(s) of interest. It is also possible to generate a mass spectrum from the impact events, in each of which only a certain number of a specific ion is detected. (e.g. a mass spectrum with the events containing only 1 Au_1^+ detected) The application of this feature is discussed in Chapter 5.

3.8   Coincidence analysis and surface coverage

A specific ion of interest can be selected in the total mass spectrum. Because each impact is detected individually, it is possible to select the subset of the impact events containing the ion of interest. The result is a coincidence mass spectrum which consists of other extracted ions, co-emitted and therefore co-localized with the ion of interest. For the Au_{400} impact, a typical desorption volume for co-emission ions is $\sim 10^3$ nm^3.[7] Figure 3.8 shows how the events are selected and what a coincidence mass spectrum contains. As discussed in Chapter 2, a large collection of nanoparticles likely contains subsets of like-nanoparticles. Here the impact events from the like-nanoparticles can be extracted from the coincidence mass spectrum with the known ion coming from these nanoparticles.

The total yield of an ion A, for any kind of sample, is calculated as follows:

$$Y_{t,A} = \frac{I_A}{N_0} \tag{3.17}$$

where $Y_{t,A}$ is the total yield of the ion A, I_A is the total intensity of the ion A, and

N_0 is the number of total impacts.

For an inhomogeneous sample surface, for example, a sub-monolayer nanoparticles deposited on graphene (Figure 3.9), we define the number of effective impacts, N_e, as the number of impacts on the nanoparticles. Therefore, for the ions A and B, which are exclusively emitted from the nanoparticles, their effective yields, $Y_{e,A}$ and $Y_{e,B}$, can be calculated as follows:

$$Y_{e,A} = \frac{I_A}{N_e} \tag{3.18}$$

$$Y_{e,B} = \frac{I_B}{N_e} \tag{3.19}$$

The effective yield of co-emitted A with B, $Y_{e,AB}$, can be calculated in the same way:

$$Y_{e,AB} = \frac{I_{AB}}{N_e} \tag{3.20}$$

where I_{AB} is the intensity of ion A in the coincidental mass spectrum with ion B (or vice versa).

Assuming in each single impact, the emission of ion A and B are independent, we have:

$$Y_{e,AB} = Y_{e,A} Y_{e,B} \tag{3.21}$$

$$\frac{I_{AB}}{N_e} = \frac{I_A}{N_e} \frac{I_B}{N_e} \tag{3.22}$$

From Eqs. 3.21 and 3.22 we have:
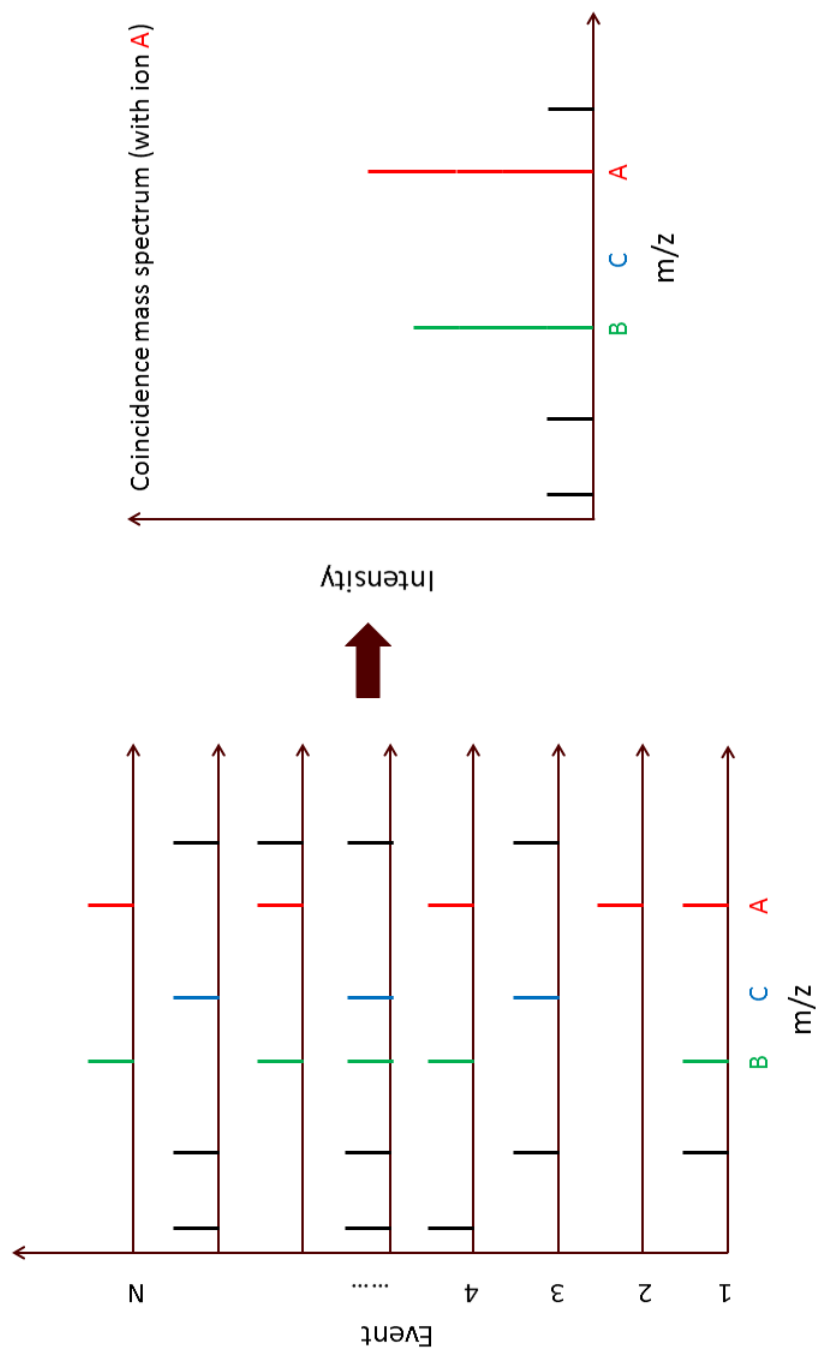
Figure 3.8: The coincidental ion mass spectrum generated from the total ion mass spectrum.
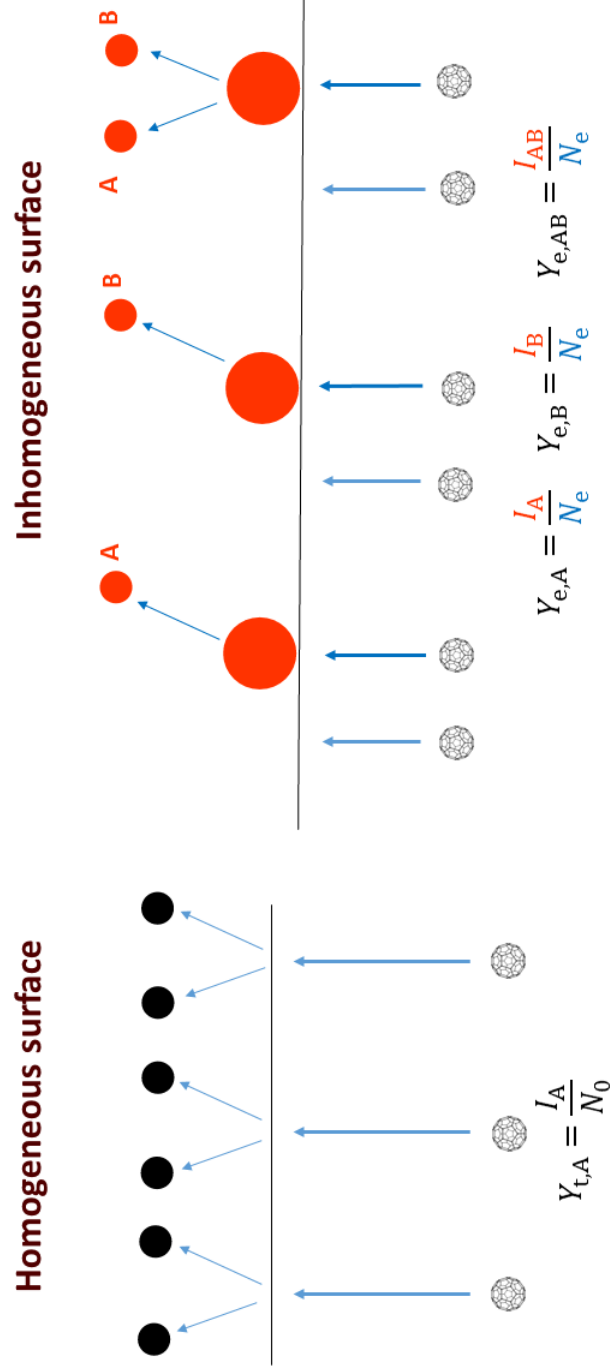
Figure 3.9: Effective yield and number of effective impacts from an inhomogeneous surface.

$$N_{\mathrm{e}} = \frac{I_{\mathrm{A}}I_{\mathrm{B}}}{I_{\mathrm{AB}}} \tag{3.23}$$

It is likely that the impact positions on a sample surface is random. Therefore the surface coverage ($K\%$) of a species, can be calculated by taking the ratio of the number of effective impacts on this species to the number of total impacts on the sample surface:[34, 41]

$$K\% = \frac{N_{\mathrm{e}}}{N_0} = \frac{I_{\mathrm{A}}I_{\mathrm{B}}}{I_{\mathrm{AB}}N_0} \tag{3.24}$$

It should be noted that in the calculation above, the ions A and B selected are emitted exclusively from the same kind of nanoparticles.

3.9   Sample preparation

The graphene used in this study were 1 layer (1L), 2 layers (2L) and 3-5 layers (4L) free-standing graphene films deposited on ∼100 nm thick[42] lacey carbon frames supported by 300 mesh standard 3.05 mm copper TEM grids (Ted Pella, Redding, CA). The graphene are in part naturally oxidized to have functional groups containing H and O on its surface. The typical coverage of the graphene is 70-90% (verified by SEM, see chapter 6). It should be noted that in the transmission direction, start signals of ToF mostly come from the impacts on the graphene film: the projectile directly going through the void area doesn't generate start signal, and the ∼100 nm lacey carbon frame is too thick for the penetration of the projectiles. The signals coming from the grazing impacts of the lacey carbon contribute $< 1\%$ of the total signal.[43]

The grids were glued on a sample holder with a ϕ 2 mm hole using silver print (MG Chemicals, Surrey, B.C., Canada). The sample holder used for C_{60} and Au_{400}

instruments are shown in Figure 3.10.

The deposition of sub-monolayer Au nanoparticles on graphene is described in Chapter 6.

Figure 3.10: Sample holders for (a) Au_{400}-SIMS instrument and (b) C_{60}-SIMS instrument. The graphene grids are glued on ϕ 2 mm holes with silver print.

4. SECONDARY ION AND SECONDARY ELECTRON EMISSION FROM C_{60} IMPACT ON GRAPHENE*

4.1 Introduction

There are numerous studies on secondary ion, emission from hypervelocity C_{60} impacts on bulk size solids (e.g., Refs. [44, 45, 46]). Briefly, C_{60} bombardment generates increased SI yields in comparison to those obtained with atomic and small polyatomic ions at equal velocity. The increase is attributed to collective effects and assumes solids of sufficient dimensions for complete energy deposition. When a 3D target is replaced by free-standing graphene, the confined volume restricts the collision parameters. So far, the impact of a 2D projectile on a 2D target has only been considered in MD simulations.[47] We present here experimental data on negative SI and electron emission from one to four layer graphene bombarded by C_{60}. Both occur in surprising abundance, suggesting distinct energy dissipation and ionization pathways. Our observations are compared below with MD simulations.

4.2 Experimental

The experiments were run at the level of individual C_{60} impacting at 25 keV (81.8 km/s) and 50 keV (115.7 km/s), with separate recording of SIs and electrons emitted in transmission from each collision.[35] The event-by-event bombardment-detection mode allows for the selection of specific impacts, in the present case those involving free-standing graphene at the exclusion of signals from the target holder and support. The targets consisted of 1 or 3-5 layers of graphene obtained from Ted Pella Inc.,

Redding CA. The graphene was supported by a lacey carbon film on a 300 lines/inch copper TEM grid. The support was analyzed and the contribution of observed SIs from the lacey carbon was found to be small (2 orders of magnitude lower).

The data were acquired with a custom-built cluster-SIMS instrument consisting of a C_{60} effusion source, a 1.2 m linear time-of-flight mass analyzer, ToF, and an electron emission microscope, EEM. Distinct features are bombardment at normal incidence and detection of SIs and electrons in the transmission direction. A detailed description of the components and data acquisition processing scheme can be found in Chapter 3. As noted earlier, the impact energies of C_{60}^{+} and C_{60}^{2+} were 25 and 50 keV respectively. To achieve event-by-event bombardment-detection conditions, the experiments were run at $\sim$1000 impacts per second. The negative SIs were identified via ToF-MS. The individual electrons were magnified and visualized in the EEM and recorded with a fast CMOS camera. Thus, for each projectile impact, a frame was acquired by the camera displaying the individual electrons with the coincidental identification of the SIs. The signals from 10^5 to 10^6 impacts were summed to generate a mass spectrum and an electron probability distribution.

4.3   Results and discussion

The mass spectra of negative ions emitted in the transmission direction contain peaks of C_n^- clusters ($n \leq 10$), molecular ions of $C_nH_x^-$ ($x = 1, 2$) and O^-. The presence of O^- and $C_nH_x^-$ in the spectra implies that the graphene is partially oxidized and has contaminants due to exposure in air prior to the experiments in vacuum. The odd-even oscillation of the yields of C cluster ions (Figure 4.1) correlate with the oscillations of C cluster electron affinities.[48, 49] They are relevant for the electron exchange mechanism involved in cluster ionization (discussed below). The high yield of C_1^- from C_{60} bombardment is in part attributed to fragmentation of the projectile.

An intriguing result is the abundant emission of carbon clusters. The yields for C_n^-, with $n \geq 3$, are dominated by small clusters and decrease exponentially with n. A similar trend was observed in bombardment of one and four layer graphene with 520 keV Au_{400}^{4+}.[9] Further, as reported earlier with Au_{400}^{4+}, a fourfold increase in target thickness resulted in only a small increase in ion yields upon bombardment with C_{60}.

The fullerene-on-graphene data exhibit in the low mass area the distinct characteristics of impacts on an extremely confined volume. C_1^-, O^-, C_2^- are emitted with a range of kinetic energies. The case of C_1^- (which includes C_1^- from fragmented C_{60}) is presented in Figure 4.2 Here the kinetic energies extend up to 1/60 of the projectile energy. It should be noted that the maximum kinetic energies of O^- and C_2^- could not be determined as their respective high energies cause overlaps in flight times with lower mass species.

For insight into the spatial origin of the ejecta, we compare the experimental observations with MD simulations. Briefly, the method consists of solving the Hamilton's equations of motion for all the atoms in the modeled system. The forces among the atoms are derived from a blend of pairwise and many-body empirical potentials.[50] Since this particular system includes only carbon atoms, all the interaction can be described by a single potential, namely AIREBO.[51] The lateral size of the modeled system was 399.11 Å×399.16 Å, with a total number of 245152 atoms. As in the experiment, the impacting C_{60} projectile was directed normal to the surface of the substrate with an initial kinetic energy of 50 keV. To obtain statistically reliable results, the total of 25 simulations have been run for 25 different impact points. Each of these simulations was stopped at 20 ps, since their further development had no significant impact on the final result. The MD simulations confirm that the atom-atom collisions in the impact region cause sputtering of carbon atoms and dimers with kinetic energies up to $E_o/60$ (Figures 4.3 and 4.5) and that
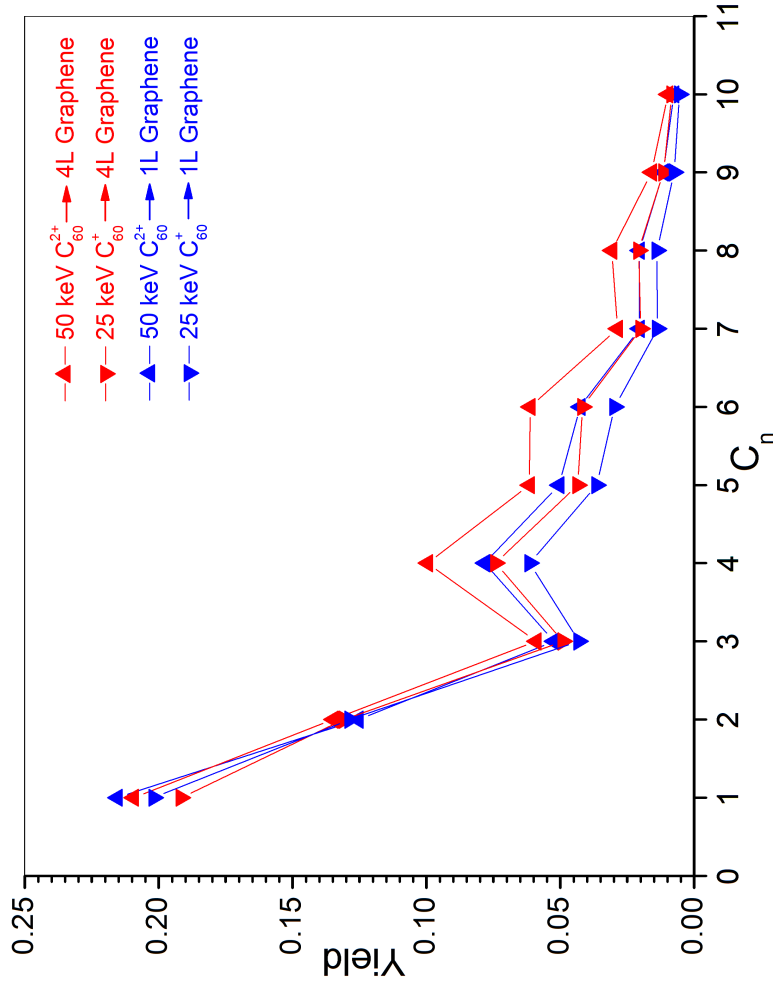
Figure 4.1: Yield of carbon clusters C_n^-, emitted from 1-Layer Graphene (blue color) and 4-Layer Graphene (red color). Accuracy in the experimental data (signal to noise ratio) is ~0.1% for the atomic ions, ~0.2% for dimers, ~0.4% for 3 $\leq C_n^- \leq 8$, and ~0.8% for the clusters C_9^- and C_{10}^-.
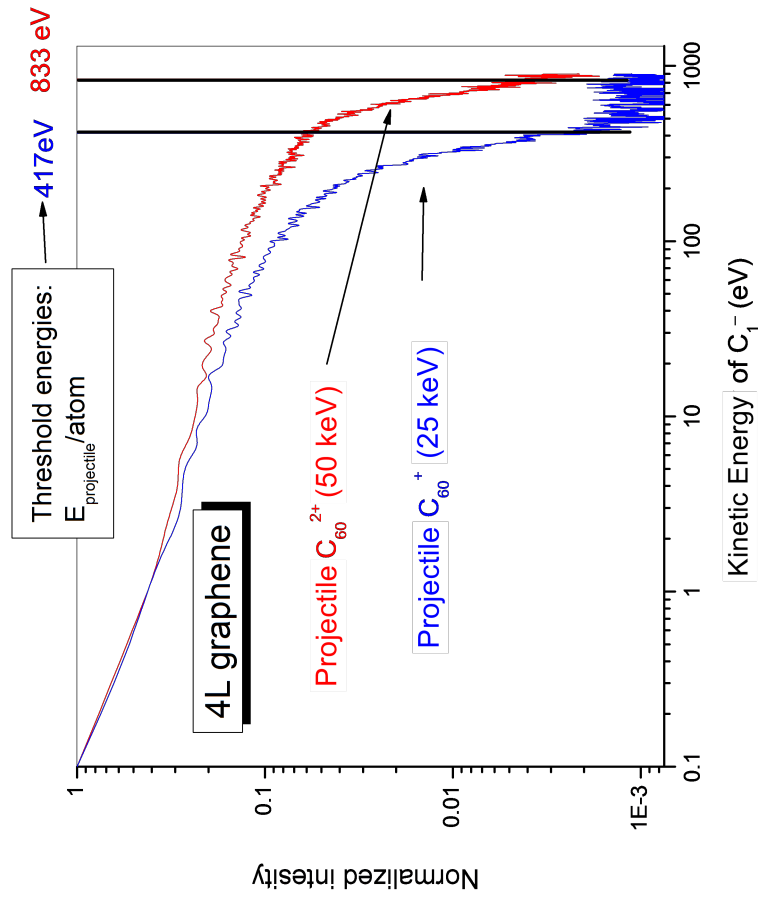
Figure 4.2: Kinetic energy distributions of C_1^- emitted by impacts of fullerenes. The distributions show that doubling of the energy of C_{60} projectile from 25 keV to 50 keV doubles the maximum energy of the emitted C_1^- from 416.5 eV to 833 eV.

the clusters are sputtered from the rim.

The atom-atom collision is a fast process ($t < 1$ ps). The projectile is atomized via atom-atom collisions. Atoms from the projectile can be ejected into the transmission direction together with knocked on atoms of graphene. For instance, in the case of 50 keV C_{60}^{2+} impacts on 4 layer graphene in the transmission direction, the yield of C_1^0 from the projectile is 35.5 atoms/projectile, which is 59.2% of total number of atoms in the projectile, corresponding to 15.5% of the total yield of carbon atoms. The MD simulation shows a post collision process ($t \approx 10$ ps), where vibrational energy accumulates around the rim of the impact hole. This energy in the rim of the hole causes sputtering of carbon clusters. Although the energy accumulated around the hole is small (a few percent of the total energy), it is sufficient for the sputtering of carbon clusters due to the confined dissipation in the 2D material. The sputtering of clusters from a confined volume differs from that in bulk, where the energy of the projectile is completely absorbed over its range and only a fraction is spent on sputtering.[52]

The ion emission prompts the issues of the ionization probability and ionization mechanism(s). Regarding C_1^-, its formation via atom-atom collisions, i.e. C_1^0 + $C_1^0 \rightleftharpoons C_1^+ + C_1^-$, is unlikely given the high barrier of activation. It should be noted though that collisions occurring within graphene-fullerene may generate quasi-molecular states, which could hypothetically create ions.[53]

The ionization probability of carbon clusters, P_n, can be estimated by comparing the experimental ion yields, $Y_{C_n^-}$, with those of neutrals, $Y_{C_n^0}$, obtained by MD simulation (Table 4.1). Figure 4.4 shows that P_n increases exponentially with the size of the carbon cluster. A notable feature of this relationship is the odd-even oscillation which correlates with the electron affinities of the respective clusters. Similar behavior has been observed in the emission from bulk carbon.[48] Electron tunnel-

38
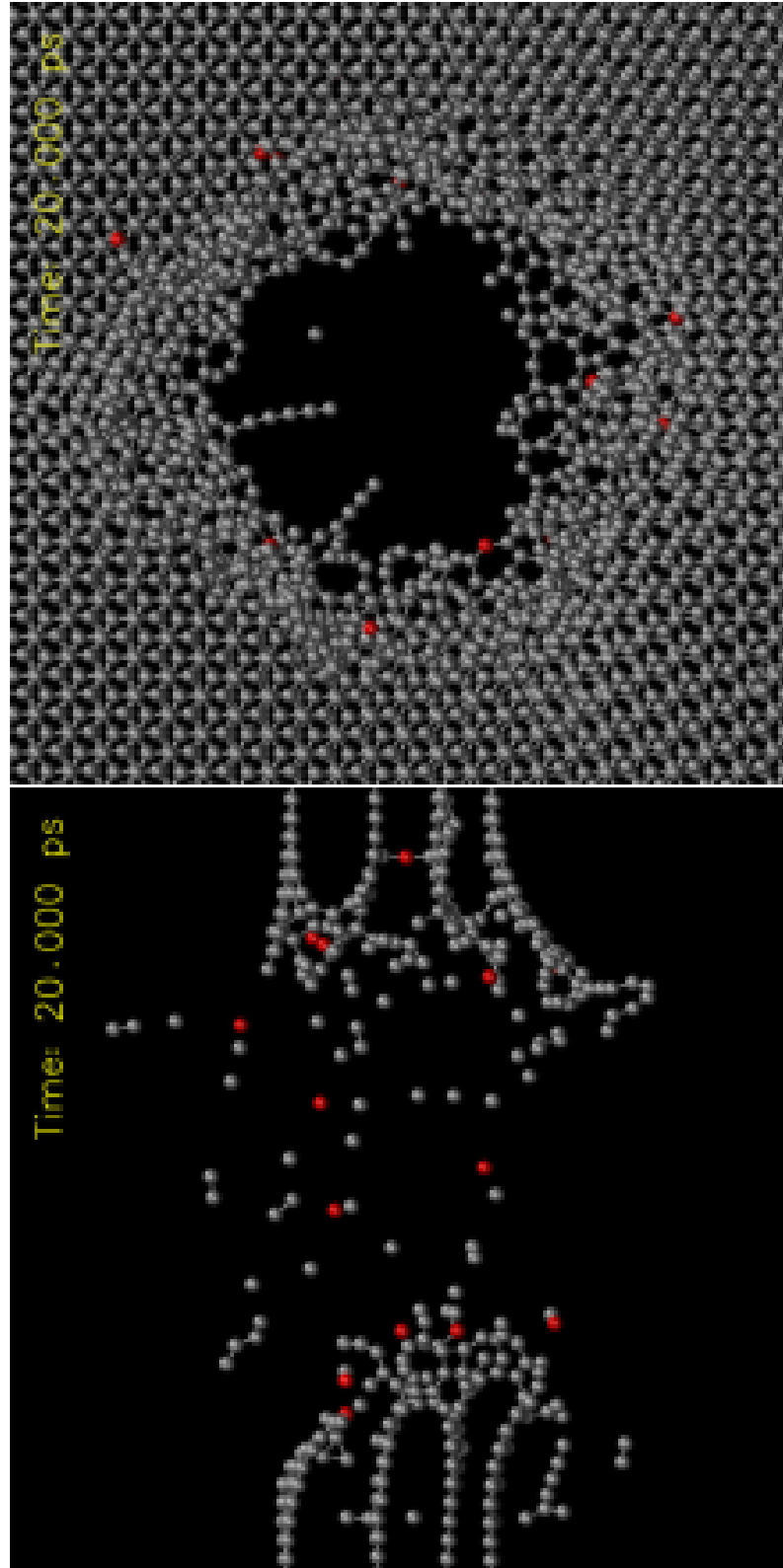
Figure 4.3: MD simulation side & top views of post-impact of 50 keV C_{60} on 4L graphene 20 ps after impact.

Table 4.1: Yields and experimental ionization probabilities of carbon clusters as a function of cluster size.

Carbon cluster	EA (eV)	Yield of ion, $Y_{C_n^-}$	Yield of neutral, $Y_{C_n^0}$	Exp. ionization probability, $P_{exp} = \frac{Y_{C_n^-}}{Y_{C_n^0}}$
C_1	1.26	0.21	228	0.0015
C_2	2.82	0.13	58.5	0.004
C_3	1.53	0.06	14.8	0.007
C_4	3.52	0.10	3.23	0.052
C_5	2.49	0.062	0.77	0.136
C_6	4.16	0.063	0.23	0.452

ing from a bulk surface to sputtered species is usually invoked as the ionization mechanism.[54, 55] The applicability of this mechanism to the case at hand may be evaluated as follows. The knocked-on carbon atoms, along with those from the shattered projectile and the clusters from the rim of the hole, are within the vicinity of the impact site for $\sim 10^{-14}$ s before they escape beyond the critical distance (~ 1 nm) for electron tunneling.

In a non-adiabatic process, the probability of ionization should vary exponentially with the kinetic energy.[54] Returning to C_1^-, Figure 4.5 shows a comparison of the experimental kinetic energies for C_1^- with those of C atoms computed by MD. They are quite similar, suggesting that the ionization probability of C_1 does not depend on its kinetic energy and can thus not be attributed to electron tunneling.

However, for C_n^-, we have noted earlier (Figure 4.4) the exponential dependence of P_n with cluster size, suggesting that electron tunneling is relevant for the production of negative carbon clusters. They originate from the rim of the hole when it is vibrationally and electronically excited. Electron tunneling and P_n can then be explained with the thermal excitation model.[55] The adiabatic limit of this model
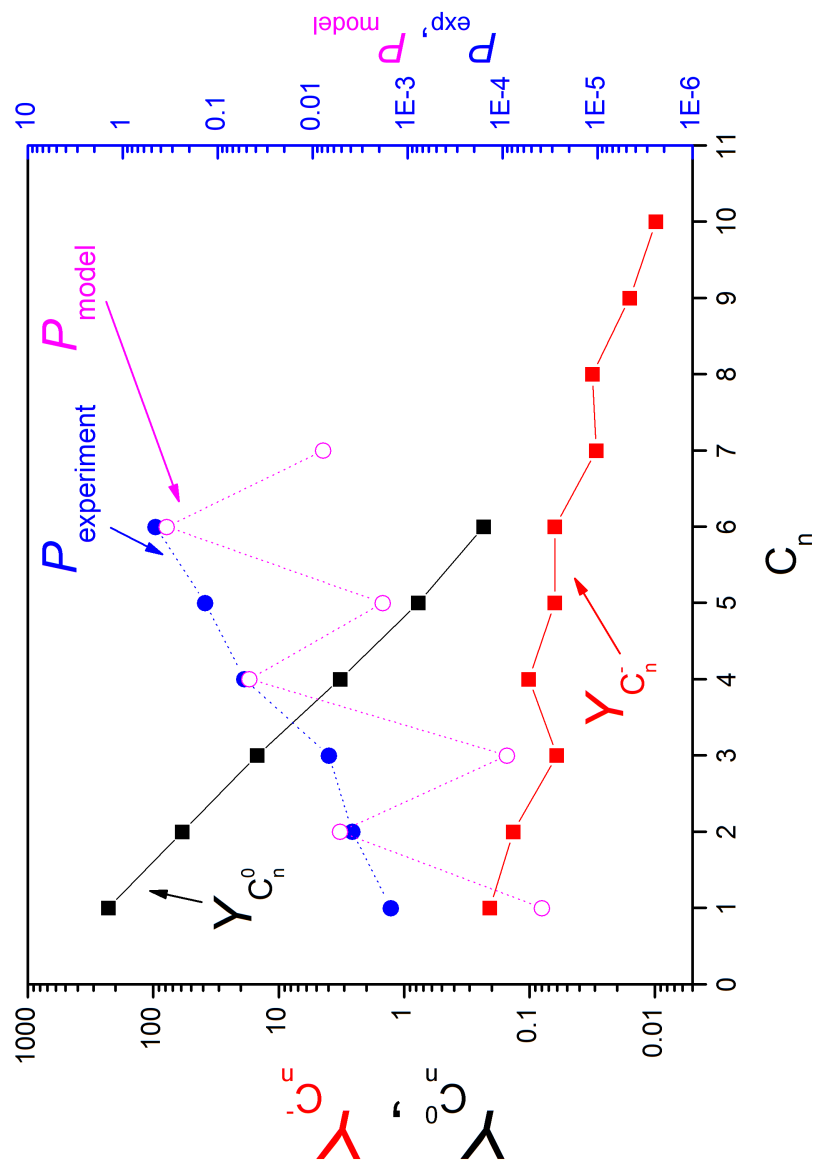
Figure 4.4: a) Yields of neutral and negatively charged carbon clusters emitted via 50 keV C_{60}^{2+} impacts on 4L graphene (left Y axis); b) ionization probabilities (right Y axis).
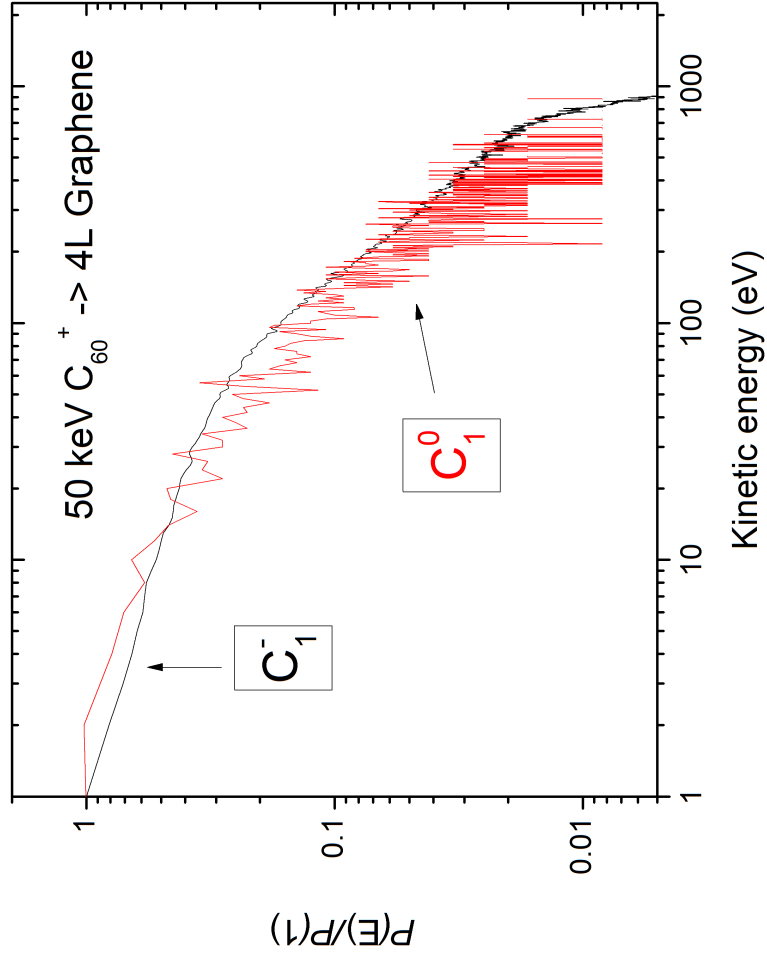
Figure 4.5: Kinetic energy distributions, for C_1^- (experiment) and for C10 (MD simulation).

can be expressed as:

$$p_n = \frac{Z^-}{Z^0}\exp\left[\frac{-(\phi - EA - \delta_{\text{ic}})}{k_{\text{B}}T_{\text{e}}}\right] \tag{4.1}$$

where T_e is the average electron temperature of the rim around the graphene hole at the time of the tunneling process, δ_{ic} is the image charge correction factor (set to zero here), Z^- and Z^0 are the partition functions of emitted C ions and neutrals at T_e. The work function of the rim is unknown, as an estimate we can take the value of the work function of the free standing pristine graphene ($\varphi = 4.5$ eV). The values obtained for the adiabatic electron affinities of carbon clusters from Ref. [49] are shown in Table 4.1. An approximation of the experimental ionization probabilities from the thermal excitation model gives an average electron temperature of 3700 K at the rim at the time of the tunneling process. The ratio of the partition functions, Z^-/Z^0, is used as a parameter of approximation ($Z^-/Z^0 = 1$). It should be noted that the carbon cluster ion yields correspond to species surviving $\sim$0.1 μs after emission (time spent by cluster ions in the extraction/acceleration region). Given that the clusters are vibrationally exited, the experimental yields incorporate the results of fragmentation and electron detachment occurring on the ejecta prior to entering the field-free drift region. These processes can explain the mild odd-even oscillations of the experimental ionization probabilities in comparison with the strong oscillations predicted by the thermal excitation model (Figure 4.4). Moreover, the temperature of 3700 K may be underestimated due to the cooling of cluster ions during fragmentation. Accurate cluster ion yields will require a correction of the experimental measurements taking into account their internal energies. An advanced methodology for determining internal energies has been described elsewhere.[56]

As a complement to the SI emissions we have also measured the emission of elec-
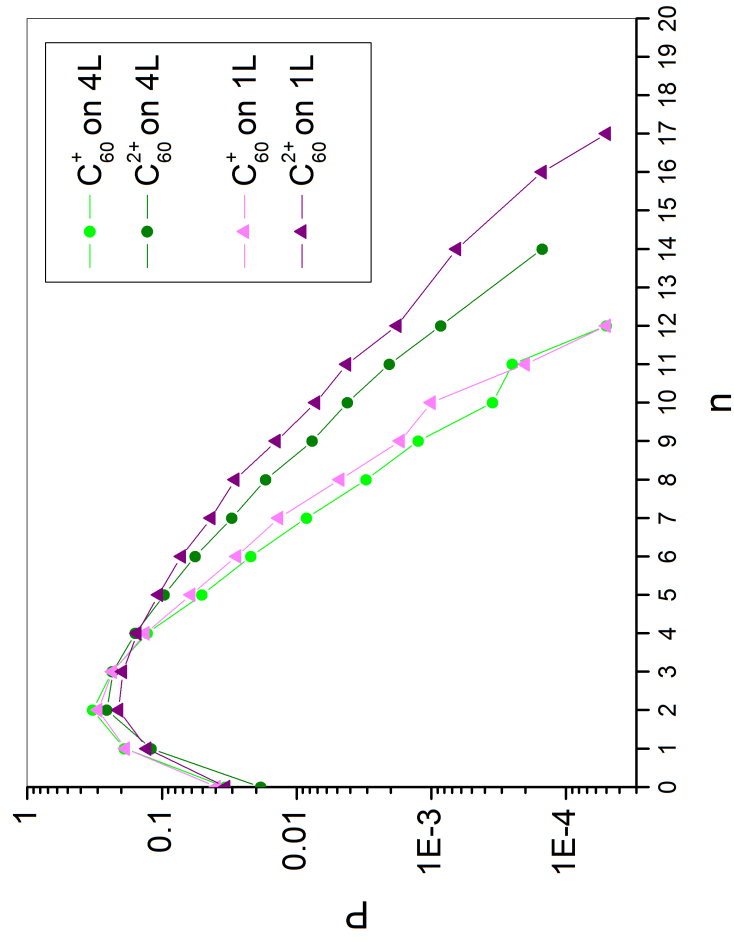
Figure 4.6: Distribution of number of electrons emitted per single impact of 25 keV C_{60}^+ and 50keV C_{60}^{2+} on 1-Layer and 4-Layer Graphene. For each distribution, the total number of collected events is 2×10^4. Standard deviation is better than $\pm 10\%$ for the events with $n \leq 10$.

trons (Figure 4.6). In our experiments, electrons are detected individually, which allows to measure the electron yields and the radial velocity distributions of the electrons.[35, 22] The electron probability distributions (Figure 4.6) are Poisson-like. On average, 3 electrons are emitted per projectile impact. The distribution of the radial kinetic energies shows that the electrons have thermal energies. The distribution of the radial kinetic energies of emitted electrons (Figure 4.7) has been measured with electron imaging detector.[33] The measured size distribution of detected electron spots was converted to the distributions of the radial kinetic energies.[22]

The surprising abundance and energetic characteristics of the electrons prompt the question of the mechanism of electron emission. The kinetic electron emission mechanism[57] cannot be invoked here, given the low velocity of the projectile. The threshold for the kinetic electron emission in the case of carbon atom-graphite interaction is 1.5×10^5 m/s.[57] The value is similar to the velocity per atom of the 50 keV C_{60} projectile (1.13×10^5 m/s) and is thus inadequate to explain the abundant electron emission. The thermal energies of electrons infer a mechanism of emission similar to thermionic emission from hot metals. Indeed, we show above that the thermalized excitation model explains the emission of negative cluster ions from 2D matter, a similar approach can be used for the emission of electrons. We can estimate the electron yield from the excited rim around the graphene hole, using a modified Richardson-Dushman law:

$$Y_e = \frac{1}{q}(\delta t \Delta S) A_0 T^2 \exp\left(\frac{-\varphi}{k_B T}\right) \tag{4.2}$$

where $A_0 = 1.5 \times 10^5$ A/m^{2}K^2 is the Richardson constant, q is elementary charge, δt is the time range of the electron emission process, ΔS is the annular surface area of excitation around hole, and T is the average temperature of this area around the
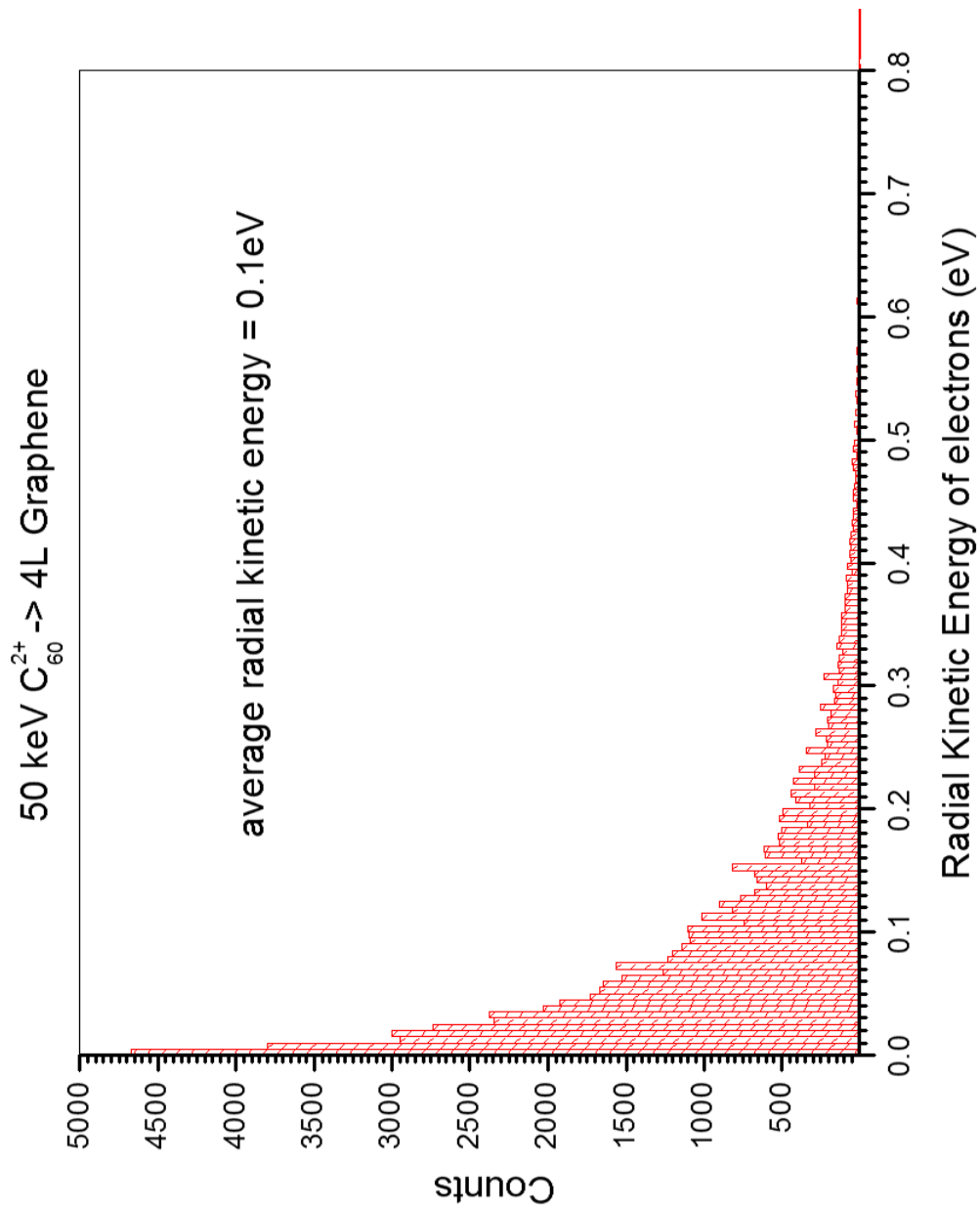
Figure 4.7: The distribution of radial kinetic energies of emitted electrons. The electrons are emitted by impacts of 50 keV C_{60}^{2+} on 4 layer graphene. The average energy of the electrons is 0.1 eV.

hole at the time of electron emission. Using the MD simulation, we estimate the value of ΔS with internal and external radii, $r = 1.5$ nm, $R = 3.0$ nm, thus $\Delta S = 20$ nm^2.[45]

The MD simulation gives a time of effective vibrational excitation in the rim of $\sim$10 ps. Assuming that the electron emission process has the same time range, the average temperature is $\sim$6000 K. This temperature for the exited area around hole gives a yield of $\sim$6 electrons per projectile impact. One should note that the emission of electrons has complete anisotropy, thus, assuming that the escape depth of electrons is larger than the thickness of the 4L graphene, the measured electron yield of $\sim$3 electrons per projectile impact corresponds to a total yield of $\sim$6.

Another possible mechanism of emission of electrons is electron detachment from the emitted negative atomic ions via the atom-ion collision process[58] and thermionic emission of electrons from the carbon cluster.[59] The experimental total yield of all ions emitted is $\sim$12 ions per impact for 4L graphene. Thus, hypothetically, the electrons from ions can contribute to the emission. To explore this contribution, direct measurement of the electron energy spectra will be necessary.

4.4   Conclusion

The interaction between C_{60} and graphene is fundamentally different from the 2D projectile impacting a 3D target. One characteristic is the high degree of ionization of the ejected carbon. In the present case the transfer of the projectile kinetic energy to the target atoms is maximized, yet holes are not evident suggesting a self-healing process.[60] In the set-up for transmission measurements, graphene provides a quasi-immaterial support for examining isolated small (< 10 nm) nano-objects and supramolecular assembles in the event-by-event bombardment-detection mode. The latter affords selection of impacts on nano-objects, i.e. nanoscale co-localization in a

setup maximizing emission of sample-specific ions, electrons and other spectroscopic signals.

5. SECONDARY ION EMISSION AND PROJECTILE FRAGMENTATION FROM Au$_{400}$ IMPACT ON GRAPHENE

5.1 Introduction

It is well documented that hypervelocity massive cluster projectile (e.g. Au$_{400}^{4+}$) impacts on bulk solids result in abundant emissions of secondary ions (SIs).[7, 61, 62] Recent studies show that high SI multiplicity also occurs in the impact on free-standing graphene, although the confined volume lacks sufficient dimensions for complete energy deposition.[9, 43] This suggests that the mechanism of ejection-ionization of SIs from a 2D material is different from those in bulk materials. Multiple questions arise here regarding the characteristics of the ejecta, the fate of the projectile and the energy balance of the process (internal and kinetic energies, energy loss). Relevant data are crucial for understanding how graphene ruptures and forms nanopores.[47, 63] The latter are of great interest as biosensors and ionic sieves.[64, 65, 66, 67] It may be noted also, that this mode of interaction generates excited clusters complementing laser excitation.[68]

To gain insight into the interaction, we bombarded free-standing graphene with 440-540 keV Au$_{400}^{4+}$ at 33-36 km/s. The experiments were run at the level of single projectile impacts with concurrent discrete detection of transmitted and forward emitted ions. From the observations in the transmission direction, we could obtain the characteristics of the projectiles and the SIs. They are detailed below with our understanding of the massive projectile-graphene interaction in the hypervelocity regime.

5.2   Experimental

The graphene film used in this study was a 1-layer free-standing graphene film on a lacey carbon net supported by a 300 mesh 3.05 mm copper TEM grid (Ted Pella, Inc., Redding, CA) with a coverage of 70-90% typically. The graphene was partially oxidized, containing hydrogen and oxygen. The TEM grid was fixed on a sample holder as the target of the SIMS analysis. The experiments were run on a custom-built SIMS instrument with a Au liquid metal ion source (Au-LMIS)[36] coupled to a linear time-of-flight (ToF) mass spectrometer. The Au_{400}^{4+} projectiles were selected by a Wien Filter at n/q = 100 ± 30 (full width at half maximum) and accelerated to 440-540 keV impact energy (33-36 km/s) by changing the target bias from -15 kV to +10 kV. The projectile-graphene impact angle was set at normal to obtain SIs in the transmission direction. The detector with a diameter of 40 mm was at a distance of 66 cm from the acceleration grid, thus Au projectile with <1 eV/atom of radial kinetic energy could be detected. The schematic of the Au_{400}^{4+} SIMS instrument can be found in Chapter 3. A detailed description of the instrumentation can be found elsewhere.[9] The impact rate was adjusted to ∼1000 projectiles per second with ∼ 10^6 total impact on the area with a diameter of 2 mm thus it is in the "super-static regime" where more than one impacts on the same site is unlikely.[69] The secondary electrons (SEs) are deflected by a magnetic prism and detected by the start detector as the start signal of the ToF measurement. Thus, only ions from impacts on graphene were recorded since a projectile impact on a thick support or a passage through an empty area will not generate a SE signal. The projectile fragments and SIs from each individual impact were detected by a 16-anode stop detector (Institut de Physique Nucléaire d'Orsay, Orsay, France) in the event-by-event bombardment/detection mode.[39] The data were recorded and processed using

custom-designed software, SAMPI.[40] The software allows to sum the records from all impacts or to select a specific mass range (or flight time range) of interest in the total mass spectrum. The co-emitted ions (i.e. the ions coming from the same ToF events as the ions in the selected mass range or flight time range) can then be extracted and summed, resulting in a coincidence mass spectrum.

5.3   Results and discussion

5.3.1   Transmission mass spectra of Au_{400}^{4+} impacts on graphene

Figure 5.1 (a) shows the negative ion mass spectrum of the 1-layer graphene bombarded with 540 keV Au_{400}^{4+} projectiles in the transmission direction (-15 kV target bias). The main features of the mass spectrum were the C_n^- ions ($n = 1$-10) followed by $C_nH_m^-$ ions. These ions have surprisingly high SI yields (e.g. 125% for C_2^-), which agrees with the results in the previous studies of the hypervelocity massive projectile impacting on graphene in the transmission direction.[9, 43] In the high mass range, the peaks of Au_{400} projectiles and projectile fragments of Au_{1-3}^- ions are present. These peaks are broad and centered at lower m/z ($\sim$183 for Au_1^-, $\sim$348 for Au_2^- and $\sim$505 for Au_3^-), indicating that these ions have shorter flight times and have initial kinetic energy distributions that come from the hypervelocity Au_{400} projectiles. The peak at m/z $\sim$547 appears on both positive and negative ion mass spectra, and is attributed to a surfactant from the manufacturing process of the graphene film. When the target bias was set to +10 kV, the positive ion mass spectrum consists of C_n^+ ($n = 1$-7) and $C_nH_m^+$ ions in the low mass range, and Au_{1-3}^- and Au_{400} projectile peaks in the high mass range (Figure 5.1 (b)).

5.3.2   Kinetic energy loss of the projectiles

When the target bias is set at -0.2 kV, only secondary electrons have enough energies to be detected as start signals. Accordingly, the spectrum obtained contains
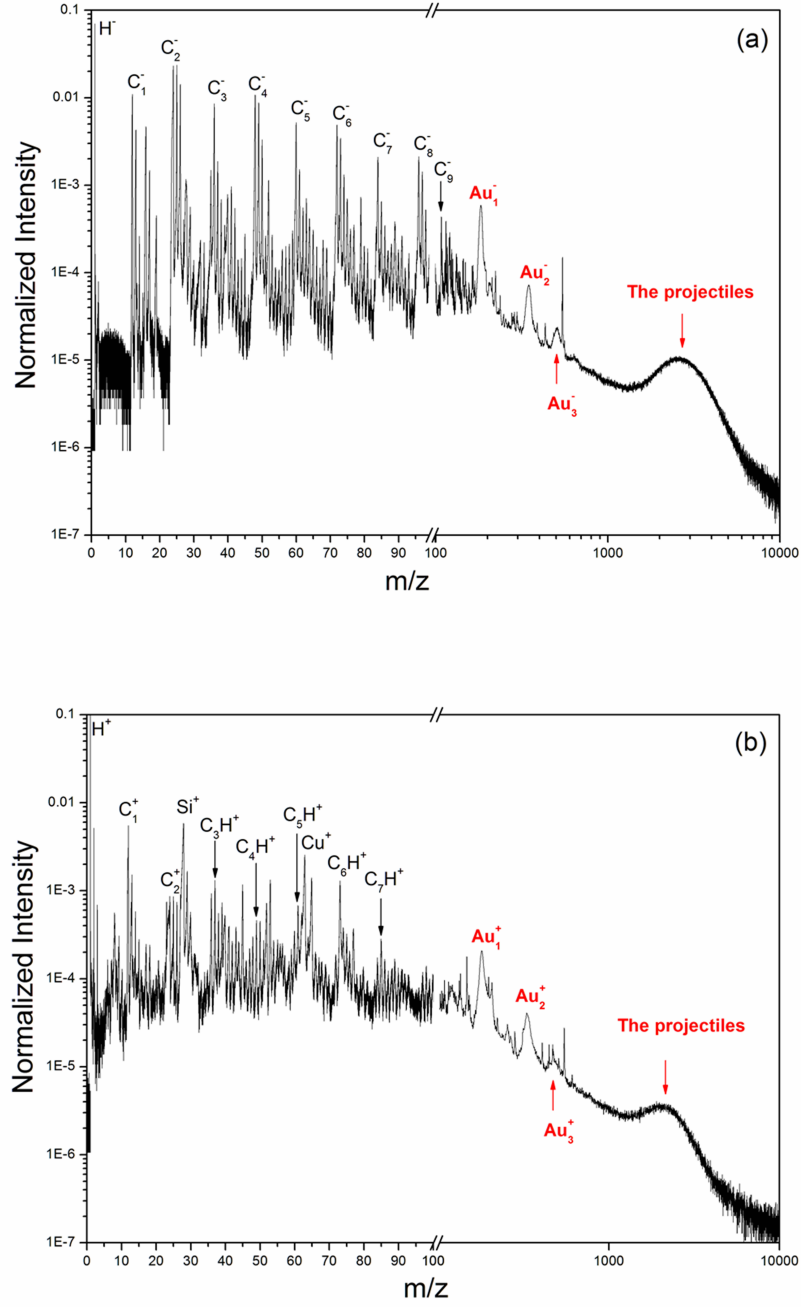
Figure 5.1: Negative (a) and positive (b) ion spectra of 540 keV and 440 keV Au_{400}^{4+} projectile impacts (-15 kV and +10 kV target bias) on graphene in the transmission direction. (The time bin is 120ps/channel. The peak heights are normalized to the total number of impacts.)

only Au_{400} projectiles without any secondary ions. The flight time distributions of the projectiles after the impact are shown in Figure 5.2. The detection/transmission efficiency here is ∼0.4, estimated from the number of Au projectiles detected in each individual impact, which is the yield of Au projectiles when the target bias was set to -0.2 kV. The wide peak of the projectile is because of the Wien filter used for mass selection ($n/q = 100 \pm 30$). The charge of the projectiles after the impact, which will be discussed later on, also contributes to the distribution of the projectiles. The fragmentation tail of Au_1^- is highlighted in red.

The kinetic energy distributions of the projectiles after the impact can be converted from the flight time distribution. By comparing the exit energy to the initial kinetic energy of the projectile (480 keV, i.e. 1.2 keV/atom) in Figure 5.3, we found that the kinetic energy loss of the projectile during the projectile-graphene interaction is $\sim 0.18 \pm 0.06$ keV/atom ($\sim 72 \pm 24$ keV/projectile, 15% of the total impact energy). This energy loss is surprisingly high. From a previous study we know that the average diameter of the hole on 1-layer graphene generated by a Au_{400}^{4+} projectile impact is 8.9 ± 1.8 nm.[9] which is much larger than the diameter of a Au_{400}^{4+} projectile (∼2 nm)[70, 71]. Breaking of all C-C bonds in the hole would require ∼18 keV. This is an upper limit because not all C-C bonds are cut since carbon clusters are observed. Additionally, there is a collision energy loss. Two hypotheses can be considered: a) assume all Au-C atom collisions are perfect elastic collision with impact parameter of 0°, resulting in a maximum energy loss of ∼35 keV; b) most collisions will not be elastic, this case has been considered in Reference [9], using SRIM (Stopping Range In Matter)[72] software, the kinetic energy gained per carbon atom is ∼100 eV, resulting in a total projectile energy loss of ∼13.5 keV. Thus, overall we cannot explain the observed energy loss (72 keV). This implies additional energy absorption over a large area of the graphene layer.
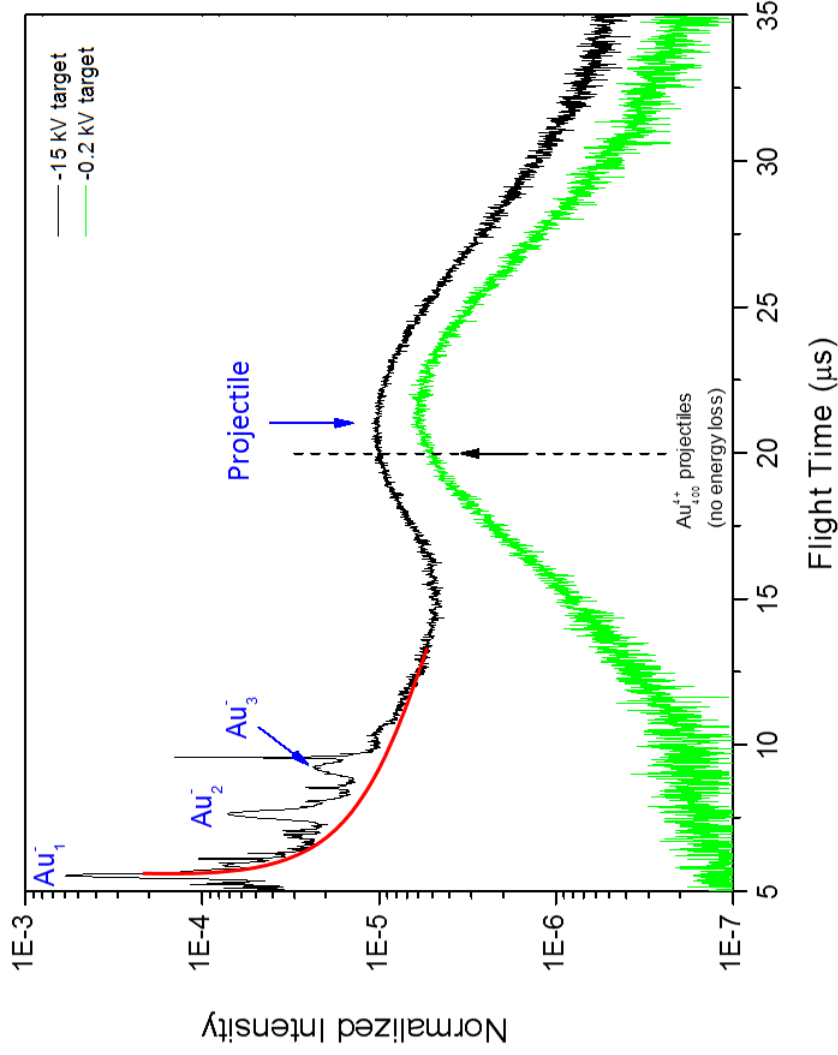
Figure 5.2: Negative ion mass spectra of 540 and 480 keV Au_{400}^{4+} projectile (-15 and -0.2 kV target biases) impacts on graphene in the transmission direction. The peaks of Au_{1-3}^- have the fragmentation tail, which are overlapped and extended up to the parent projectile peak. The red line is for eye-guiding (peak height is normalized by the total number of impacts).
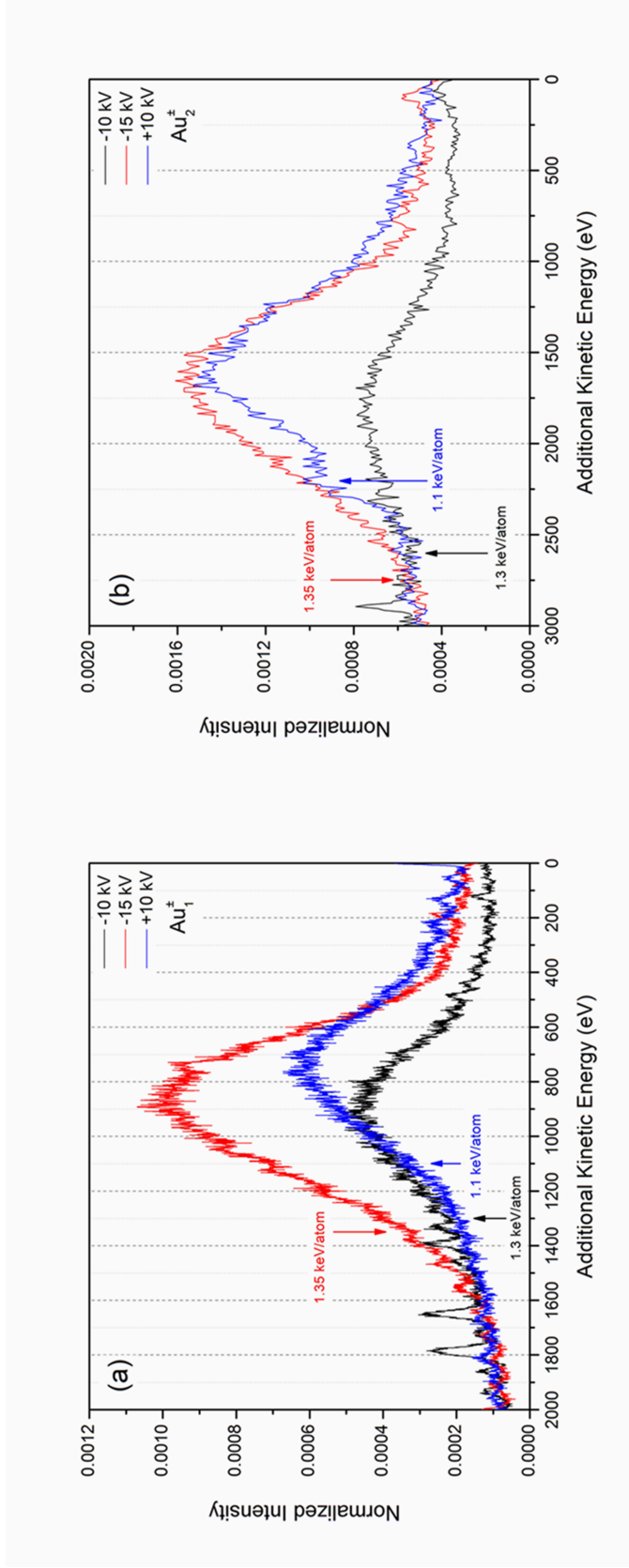
Figure 5.3: $Au_1^\pm$ (a) and $Au_2^\pm$ (b) peaks from the mass spectra of 540, 520 and 440 keV Au_{400}^{4+} projectile (-15, -10 and +10 kV target biases) impacts on graphene, in energy scale. The axial kinetic energies without energy deficits are labeled (peak height normalized by the total number of impacts; data binned by 1 eV for $Au_1^\pm$ and 10 eV for $Au_2^\pm$).

As discussed above, we also found that $Au_{1-3}^{\pm}$ peaks are broad (due to the distribution of their parent projectiles), have fragmentation tail at the right half due to the fragmentation of their parent projectiles, and have energy losses due to the energy losses of their parent projectiles during the impact (Figure 5.3). Figure 5.4 shows the schematic of the fragmentation of the projectiles in the acceleration region and the present of the corresponding peaks in the mass spectrum. In the acceleration region between the biased target and the first grounded grid in the transmission direction, the projectiles evaporate Au atoms and small clusters ($Au_{2,3}$) which are partially ionized (see the discussion below). The $Au_{1-3}^{\pm}$ ions are accelerated only from the point they are generated to the grounded grid, which explains the tails on the right side of the $Au_{1-3}^{\pm}$ peaks.

5.3.3   Total and coincidental secondary ion yields of the $Au_{1,2}^{\pm}$ ions

Table 5.1 shows the experimental total yields of the $Au_1^{\pm}$ and $Au_2^{\pm}$ ions with different target biases, obtained from the corresponding mass spectra. Considering the ionization probability of the Au_{1-3} ions and the flight time of the projectiles in the acceleration region (430-470 ns), it is reasonable that multi-step fragmentation processes occur, and the total SI yields of the $Au_{1-3}^{\pm}$ ions are the sum of the SI yields of the evaporated and ionized $Au_{1-3}^{\pm}$ ions from each steps before the projectile enters the field-free space (where the $Au_{1-3}^{\pm}$ daughter ions will have the same flight time as their parent projectiles, so they cannot be differentiated in the mass spectrum).

Figure 5.5 shows Au_3^+ ions in the coincidence mass spectra, with the projectiles in specific flight time ranges (+10 kV target bias). In other words, these Au_{1-3}^+ ions were emitted from the projectiles with flight times in specific time ranges (indicated in different colors in Figure 5.5). If we assume that for the projectiles with different masses and charges the energy losses during the impact are similar, the average mass-
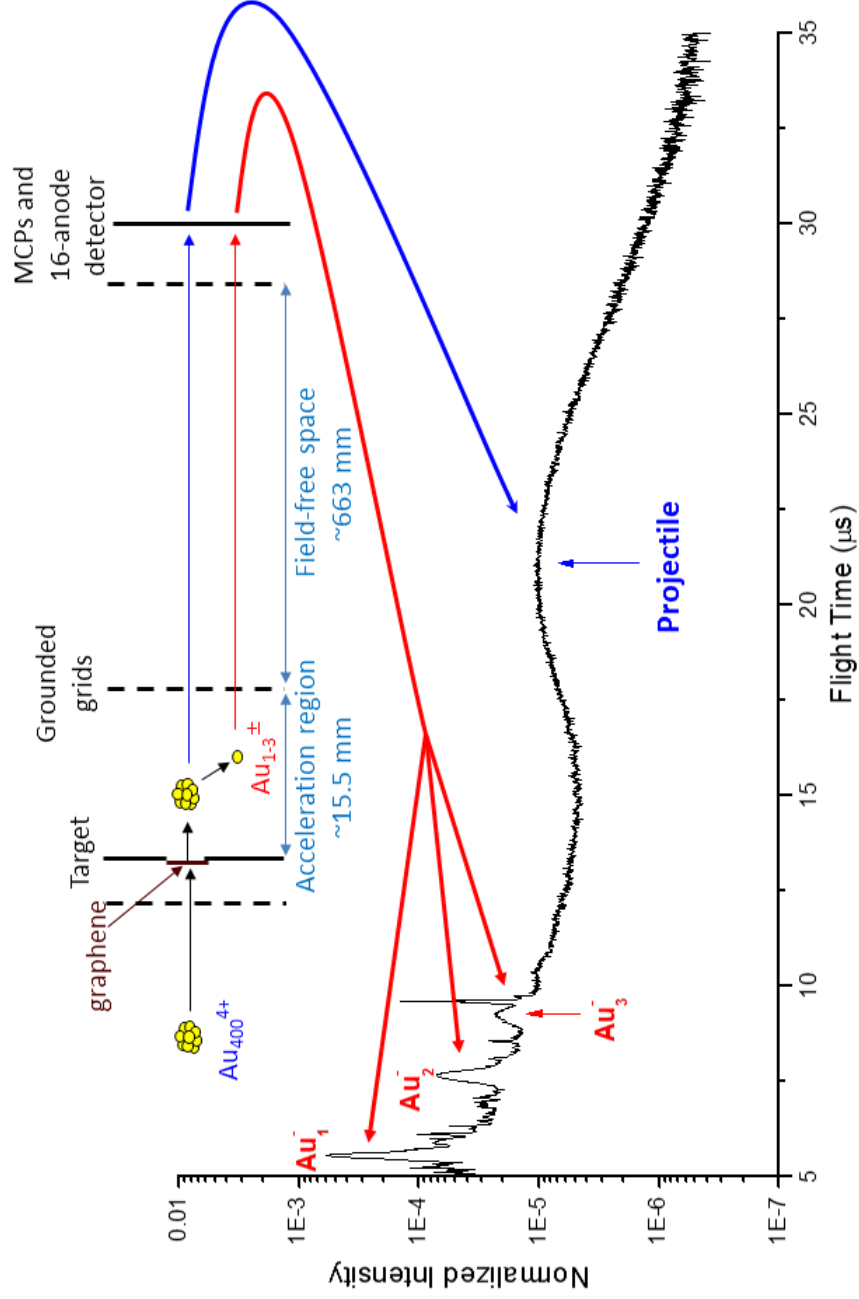
Figure 5.4: Fragmentation of the projectiles and evaporation of Au fragment ions from the projectiles in the acceleration region (peak height is normalized by the total number of impacts)

57

Table 5.1: Total experimental SI yields of the $Au_{1,2}^{\pm}$ ions with different target biases.

	Target Bias		
	+10 kV	-10 kV	-15 kV
Au_1	41%	34%	69%
Au_2	11%	2.9%	11%

to-charge ratios of the projectiles in the flight time ranges can be calculated. Here we focused on the right half of the projectile peak, because the left half is more interfered with the background thus the trend is blurred. We found that projectiles with longer flight time tend to have higher coincidental yields of Au_{1-3}^{+} ions (especially Au_3^{+}), and these ions shift to the right in the coincidence ToF mass spectra. The coincidental yield of an ion A, $Y_{c,A}$, is defined as the intensity of ion A in the coincidence mass spectrum with ion B, $I_{A,B}$, divided by the number of coincidence events with ion B, N_B:[41]

$$Y_{c,A} = \frac{I_{A,B}}{N_B} \tag{5.1}$$

Figure 5.6 shows the coincidental yield of $Au_{1-3}^{\pm}$ ion peaks with the Au projectiles within different flight time ranges. This indicates that lower velocity projectiles tend to evaporate more Au fragments, which have lower velocities on average.

Figure 5.7 shows the coincidental yields of C_n^{-} ions ($n = 1$-10) with different number of detected Au_1^{-} ions per impact event. The yields increase with the increase of number of detected Au_1^{-} ions per impact event. Indeed multiple Au_1^{-} likely originate from a larger parent projectile, which is more efficient for SI emission of small carbon cluster ions. The same effect was found in the positive ion mass spectra. More in-depth explanation of the enhancement involves the electrostatic post-interaction
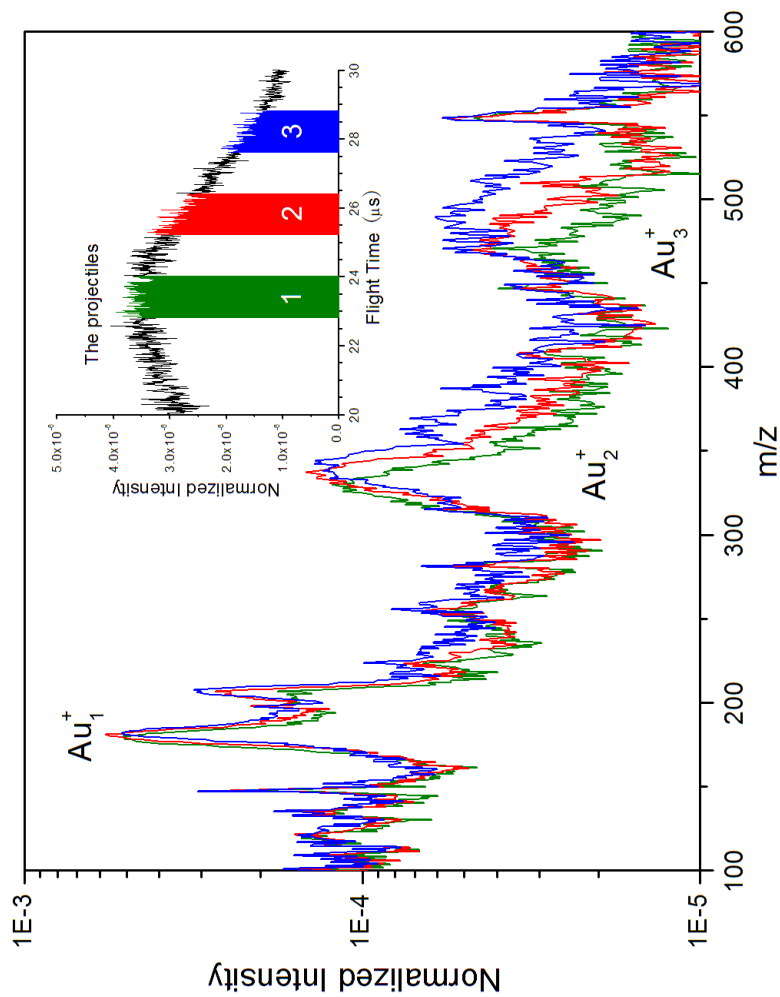
Figure 5.5: Coincidence mass spectra of Au_{1-3}^+ ions with the projectiles in different flight time ranges, from the experiment of +10 kV target bias. (peak height is normalized by the number of coincidence events, i.e. the number of selected impacts).
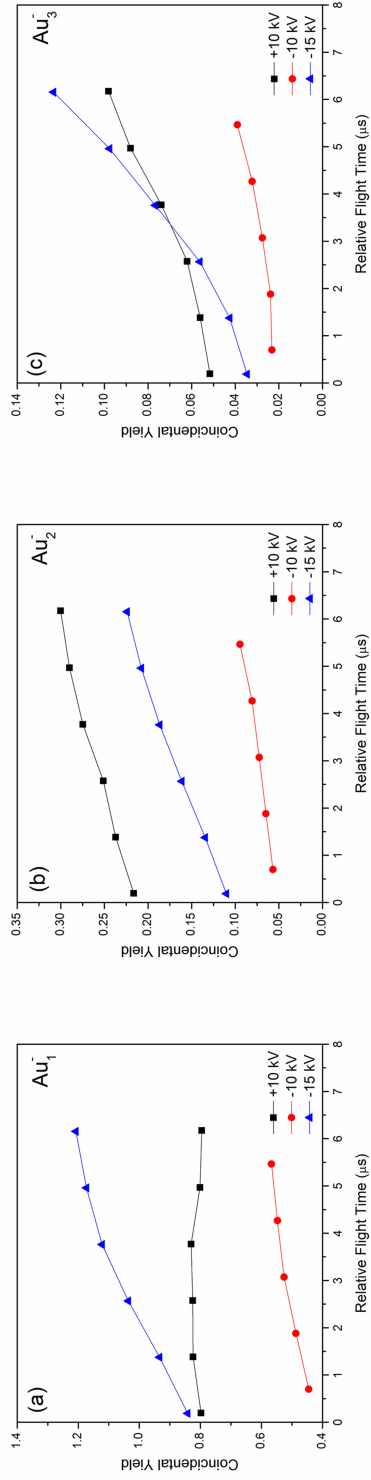
Figure 5.6: Coincidental yields of $Au_1^{\pm}$ (a), $Au_2^{\pm}$ (b) and $Au_3^{\pm}$ (c) ions from the impacts of Au projectiles within different flight time ranges (flight time is relative to the flight time at the maximum of the peak).

of the multi-charged projectile with the rim of the graphene hole (see the discussion below).

5.3.4   Fragmentation of the projectiles

A further question regarding detection of projectile, is the probability of the shattering of the projectile after impact, which may be competitive with the projectile fragmentation via Au atoms and small Au clusters evaporation. The large fragments of the shattered projectile should be detected as individual particles, which simultaneously approach the 16-anode detector.Figure 5.8 shows the distribution, $\Pi(a_{\exp})$, of number of projectile fragments, $a_{\exp}$, detected per impact event. Note that the Au atoms and small neutral Au fragments cannot be detected by MCP due to their low velocities (~ 1 keV/atom). The large fragments (tens or hundreds of atoms) are detected due to the "collective effect" when striking the MCP.[73]

From the experimental distribution, $\Pi(a_{\exp})$, we can infer the corrected distribution of number of fragments per shattered projectile, $\Upsilon(a)$ (Figure 5.8). The methodology used is that of the occupancy theory.[74] This approach was shown in details in Ref. [69]. For the 16-anode detector the equations are as follows:

$$\Pi(a_{\exp}) = \sum_{b=0}^{a_{\exp}} \left[\Psi(b|a_{\exp}) \sum_{a=0}^{b} \Phi(a|b)\Upsilon(a) \right] \tag{5.2}$$

The conditional probabilities $\Psi(b|a_{\exp})$ and $\Phi(a|b)$ are defined as

$$\Psi(b|a_{\exp}) = \frac{m!}{(m-a_{\exp})!(a_{\exp})!} \sum_{i=0}^{a_{\exp}} (-1)^i \frac{(a_{\exp})!}{i!(a_{\exp}-i)!} (1 - \frac{m-a_{\exp}+i}{m})^b \tag{5.3}$$

$$\Phi(a|b) = \tau^b (1-\tau)^{a-b} \frac{a!}{(a-b)!a!} \tag{5.4}$$
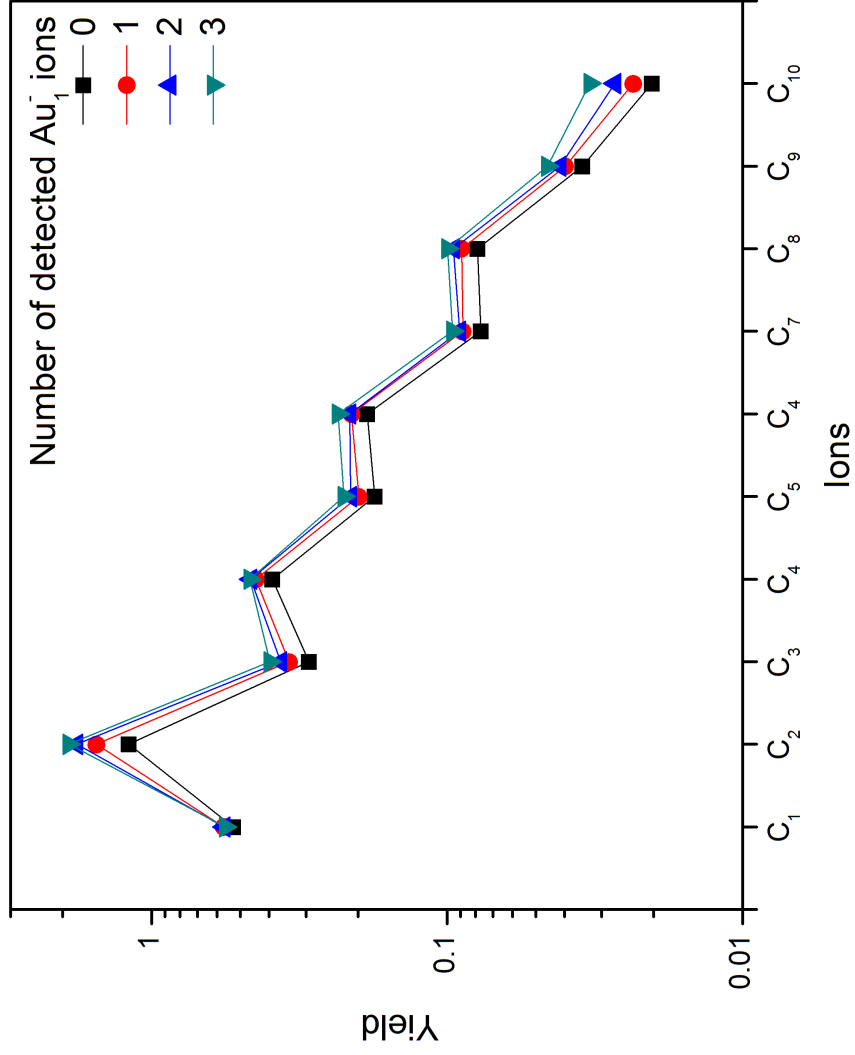
Figure 5.7: Coincidental yields of C_n^- ions ($n = 1$-10) with 0-3 Au_1^- ions detected per impact event.

where m is the number of anodes (in our case $m = 16$), $\tau = 0.4$ is the detection efficiency of MCP. Note that all impacts are random and independent.

The distribution $\Upsilon(a)$ consists of the events with only one detected large fragment of projectile ($\sim 25\%$ of all events) and the events where a few large fragments of projectile were detected ($\sim 25\%$). The events with only single detection of projectile indicate that, despite the strong excitation via impact, some of the projectiles do not undergo prompt shattering. These projectiles experience fragmentation via the evaporation of atoms and small fragments. However, a significant amount of the projectiles ($\sim 50\%$) do not survive the impact event (no fragments detected). These projectiles were completely shattered/fragmented into small fragments and atoms, which cannot be detected by MCP due to their small velocities (~ 1 keV/atom). Thus, for the calculations of the fragmentation rates we select from the total set of impact/detections, the sub-ensemble of survived projectiles, which are detected as single particles. We infer that these projectiles, after impact, experience a strong vibrational excitation which is dissipated by the process of evaporative cooling.

5.3.5 Multi-step evaporation and ionization of $Au^{\pm}$ ions

For the hot Au_{400} clusters cooling by evaporating Au atoms or small clusters (an "evaporative ensemble"[75]), the evaporation rate $k_{\text{evap}}(n)$ of an Au neutral atom can be obtained using the classical RRK expression.[76, 77, 78]

$$k_{\text{evap}}(n) = vg(n) \left[1 - \frac{D(n)}{E^*(n)} \right]^{s(n)-1} \tag{5.5}$$

where n is the number of atoms in the Au cluster ($n = 400$ initially), ν is the vibrational frequency (typically 10^{12} to 10^{13} Hz)[78], $g(n)$ is a degeneracy factor, usually equals the number of surface atoms (the number of the surface atoms for Au_{400} is estimated as ~ 196 atoms[79]), $s(n)$ is the number of vibrational degrees of

63
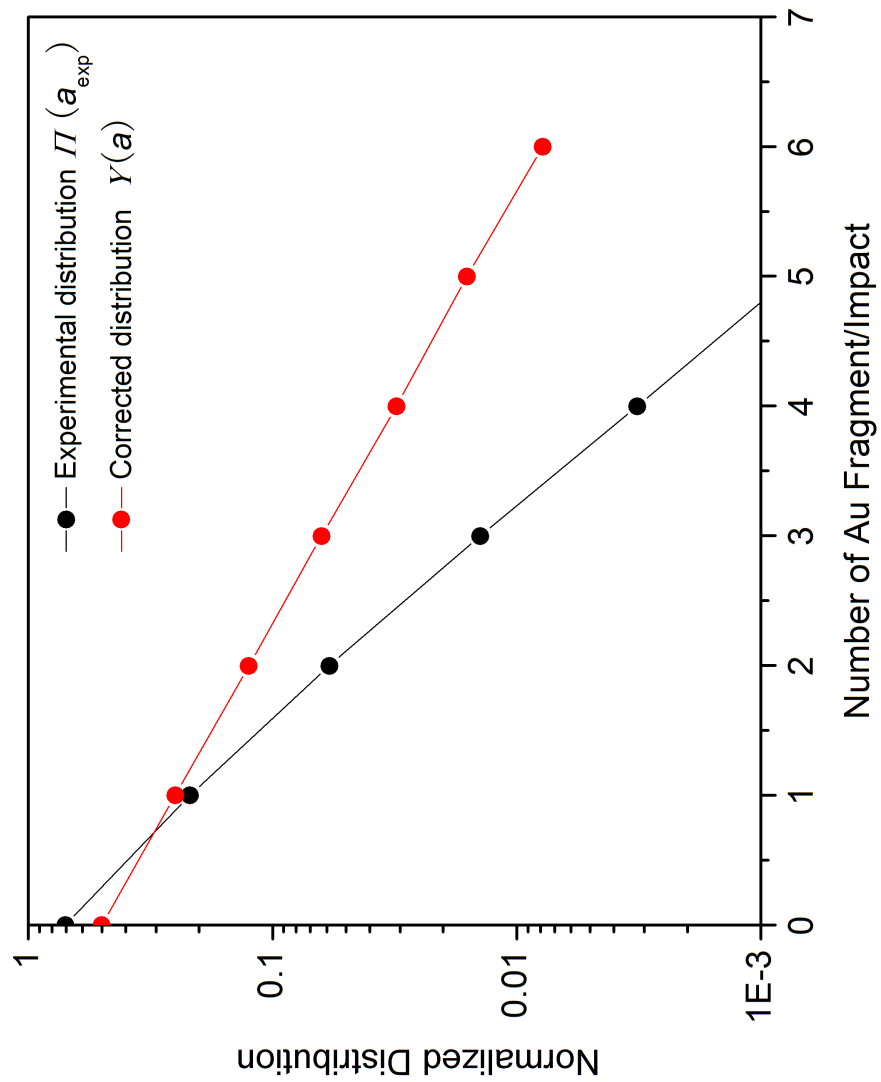
Figure 5.8: Distribution of number of projectile fragments detected per impact event.

freedom ($s(n) = 3n - 6 = 1194$), $D(n)$ is the dissociation energy needed to separate one atom from the cluster, and $E^*(n)$ is the internal energy of the cluster projectile. The size-dependent $D(n)$ can be found using the following equation:[80]

$$D(n) = E_{\text{B}}(n) = E_{\text{B,bulk}} + 2^{\frac{1}{3}}(\frac{1}{2}D_{\text{e}} - E_{\text{B,bulk}})/n^{\frac{1}{3}} \tag{5.6}$$

where $E_{\text{B}}(n)$ is the binding energy per atom of the cluster, $E_{\text{B,bulk}}$ is the binding energy per atom of the bulk metal and D_{e} is the binding energy of the dimer. For Au we take $E_{\text{B,bulk}} = 3.65$ eV and $D_{\text{e}} = 2.344$ eV.[81, 82] For Au$_{400}$, we have $D(400) = 3.23$ eV.

Since the evaporation process is a first-order reaction, the yields of the daughter ions in each steps can be calculated by using the Bateman equations which are for describing the time evolution of nuclide concentrations of a linear radioactive decay chain governed by a set of first-order differential equations. The Bateman equations are as follows:[83]

$$N(n', t) = \frac{N(1,0)}{k_{\text{evap}}(n')} \sum_{i=1}^{n'} k_{\text{evap}}(i)\alpha(i)e^{-k_{\text{evap}}(i)t} \tag{5.7}$$

where

$$\alpha(i) = \prod_{\substack{j=1 \\ j=i}}^{n'} \frac{k_{\text{evap}}(j)}{k_{\text{evap}}(j) - k_{\text{evap}}(i)} \tag{5.8}$$

where $N(n',t)$ is the number of the projectiles before the n'th step of the evaporation at time t, $N(1,0)$ is the initial number of the projectiles (i.e. the total number of impacts N_0), $k_{\text{evap}}(n')$ is the decay constant (i.e. the evaporation rate in Eq. 5.2) of the n'th step (here $n' = 400 - (n - 1)$).

From Eqs. 5.7 and 5.8 the numbers of the projectiles in each evaporation steps

at a certain time t after the impact can be calculated. Since there are n'-1 evapo-rated neutral Au atoms before the n'th step, the total number of neutral Au atoms evaporated from the projectile, N_{neu}, can be summed up using the following equation:

$$N_{\text{neu}} = \sum_{n'=1}^{n_{\text{max}}} N(n', t)(n' - 1) \tag{5.9}$$

where n_{max} is the maximum number of atoms that can be evaporated from a projec-tile. Here we take $n_{\text{max}} = E^*(400)/D(400)$. It does not mean that all n_{max} steps of the evaporation will happen, because the projectile becomes cooler and cooler and the evaporation process is slower and slower and only a certain number of steps will happen before the projectile enters the field-free space. The total number of Au ions, N_{ion}, is calculated using the following equation:

$$N_{\text{ion}} = \sum_{n'=1}^{n_{\text{max}}} \left[\sum_{i=n'}^{n_{\text{max}}} N(i, t) \right] p^+(n' - 1) \tag{5.10}$$

where $p^+(n' - 1)$ is the ionization probability of the Au atoms in the n'th step of evaporation ($n' = 400 - (n - 1)$). The Au atoms are ionized after the evaporation via electron exchange with excited parent Au projectiles. The ionization probability can be found using the following thermal excitation model of electron tunneling:[55, 43]

$$p^+(n) = \frac{Z^+}{Z^0} \exp\left[\frac{-(E_{\text{i,Au}} - \phi_{\text{Au}} - \delta_{\text{ic}})}{k_{\text{B}} T_{\text{e}}(n)} \right] \tag{5.11}$$

where $T_{\text{e}}(n)$ is the electron temperature of the projectile surface, which is approxi-mately equal to $T(n)$, the temperature of the projectile, Z^+ and Z^0 are the partition functions of emitted Au ions and neutrals at $T_{\text{e}}(n)$ (we set $Z^+/Z^0 = 1$), $E_{\text{i,Au}} = 9.23$ eV is the ionization energy of a Au atom, $\phi_{\text{Au}} = 5.47$ eV is the work function of Au,[82] δ_{ic} is the image charge correction factor (we set $\delta_{\text{ic}} = 0$ here), and k_{B} is

the Boltzmann constant. $p^+(n)$ is a function of n and ϕ_{Au}. Typically for the first evaporated Au atom, $p^+(1)$ is in the range of 0.02-0.2. In Eq. 5.11, the work function of the Au projectile, ϕ_{Au}, is affected by the charge of the projectile. The work function of a metallic sphere having Z charges can be calculated using the following equation:[84, 85]

$$\phi_{Au}(R, Z) = \phi_{Au,\infty} + (Z + \frac{3}{8})\frac{e^2}{R} \tag{5.12}$$

where $\phi_{Au,\infty} = 5.47$ eV is the work function of an infinite Au surface and R is the radius of the Au cluster. For a Au_{400} cluster, R is ~1 nm. Because we observed both positive and negative Au fragment ions in the corresponding positive and negative modes, it is reasonable that there is a wide charge distribution of the projectiles after the impact from positive to negative. We assume that the projectile is neutralized when approaching the graphene by electron tunneling, because the work function of graphene ($\phi_G = 4.5$ eV) is lower than the work function of the Au projectile (for Au_{400}, $\phi_{Au} = 6.0$ eV). Then after the impact the projectile can be partially ionized positively and negatively. The charge of the projectiles after the impact will be discussed below. We may note here a report of free-standing graphene providing "tens of electrons for charge neutralization of a slow highly charged ion".[86]

The evaporation rate of each step, $k_{evap}(n)$, is given by the RRK expression, and the number of daughter ions in each steps, $N(n',t)$, is given by the Bateman equations. Since the sum of the numbers of all daughter Au ions, N_{ion}, is the intensity of the corresponding Au peak in a time range (from the time of the impact t_0, to a certain time t), which is obtained from the mass spectrum, the number of evaporation steps and the initial internal energy of the hot parent projectile immediately after the impact on graphene can be estimated. For the +10 kV target bias case, we take

the maximum of the Au_1^+ peak as the initial time t_0, and pick a time range from t_0 to $t = 1.28 \times 10^{-7}$ s. The yield (considering a detection/transmission efficiency of ~ 0.4) in the selected range is $N_{\text{ion}}/N_0 = 0.255$. According to Eqs. 5.11 and 5.12, the ionization probability is a function of the charge of the Au projectile. The evidence of charged projectiles after the impact implies that the neutralized projectiles are partially ionized positively. Figure 5.9 shows the distribution of the number of Au^+ ions emitted from their parent projectile with only one fragment detected per impact event (likely not fragmented) in the experimental time range (from t_0 to $t = 1.28 \times 10^{-7}$ s). This distribution is obtained using the same method as that in Figure 5.7.

In the following calculation we focus on the events containing one emitted Au^+ ion each, which are dominant, and likely come from the projectiles with +1 charge (only intact projectiles are considered here). The relationship between the internal energy and the yield of Au^+ ion is shown in Figure 5.10 (a). The measured yield in the selected time range is $N_{\text{ion}}/N_0 = 0.255$. A typical range of vibrational frequencies of 10^{12}-10^{13} Hz is used in the calculation. For this range the internal energies of the projectiles are ~ 450-500 eV (4400-4900 K). At this internal energy and time range, the number of evaporation steps of the projectile in the experimental time range is ~ 90-100. This estimation is based on comparing the sum of the number of ions generated in each step using Eqs. 5.9-5.11 with the measured yield. For the projectiles with different charges (positive, negative, and neutral), the internal energies gained should be similar due to the equivalency of the impacts on the homogeneous graphene.

The same calculation can also be applied for the negative ions. When the target bias is -10 kV, we picked a time range from t_0 to $t = 1.28 \times 10^{-7}$ s (the same as that for the positive ions). The normalized peak intensity in this range is $N_{\text{ion}}/N_0 = 0.184$
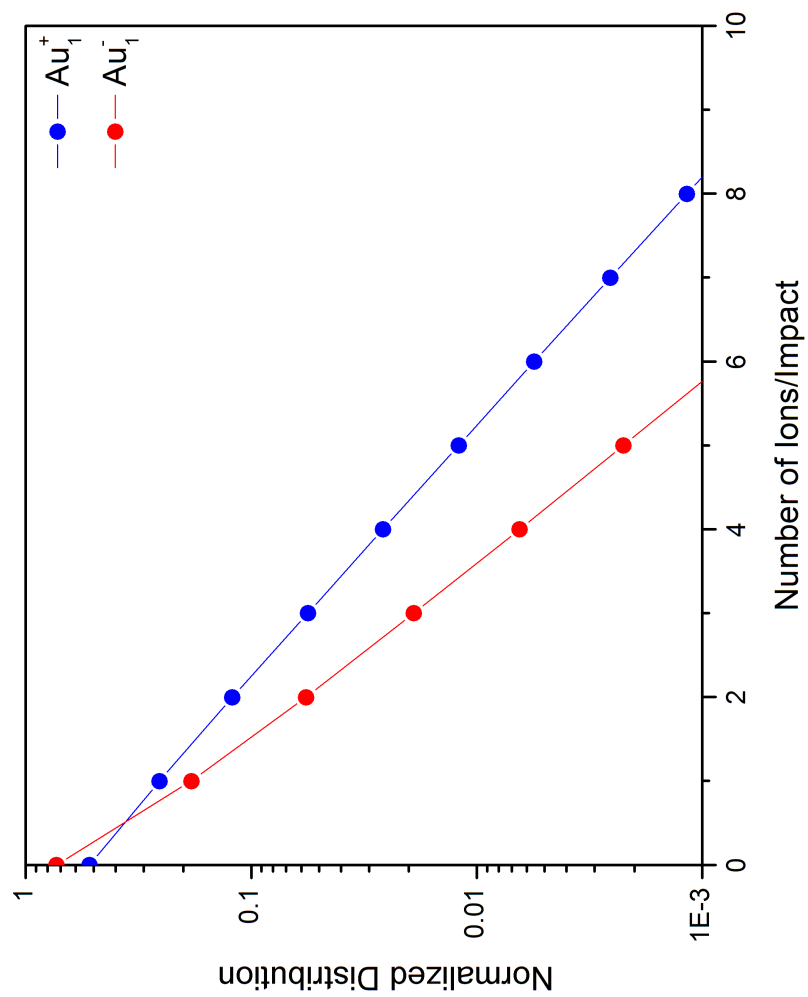
Figure 5.9: Normalized distribution of the number of $Au_1^{\pm}$ ions emitted from the selected impact event with one projectile fragment was detected in the experimental time range.
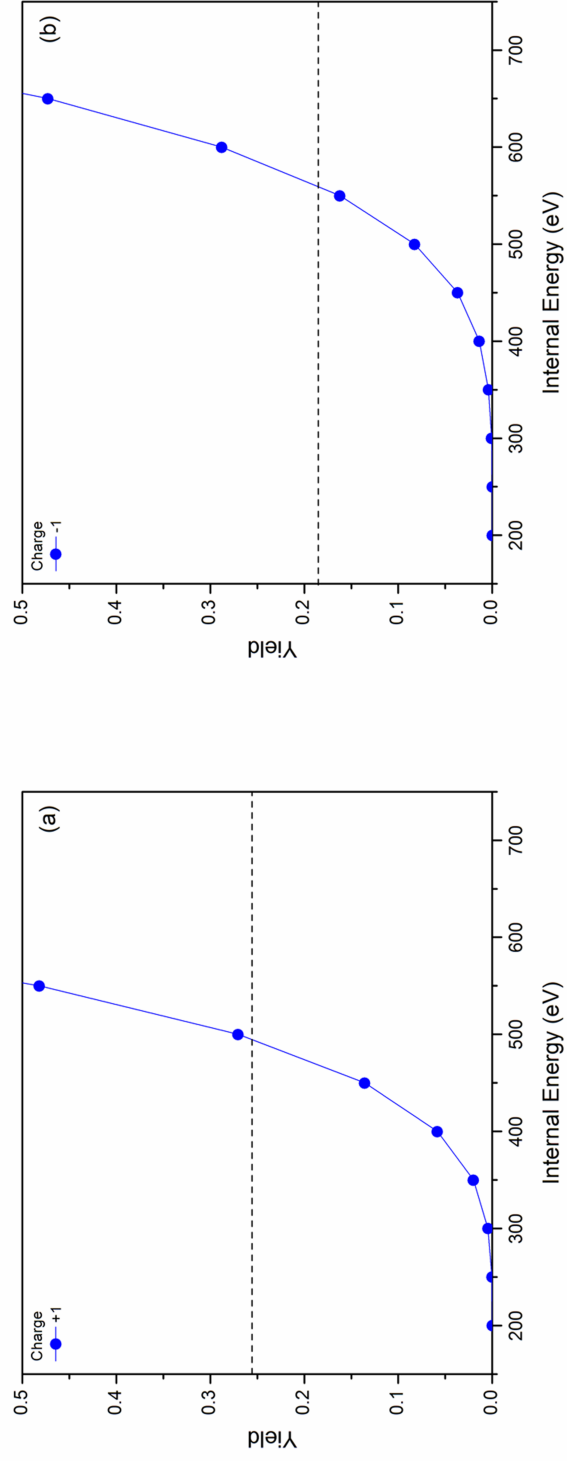
Figure 5.10: Calculated yields of Au^+ (a) and Au^- (b) at different projectile internal energies after the impact with a vibrational frequency $\nu = 10^{12}$ Hz. The horizontal dashed lines show the experimental yields of Au^+ and Au^- ions.

(considering a detection/transmission efficiency of ~0.4). Instead of Eq. 5.11 for the positive ions, the following equation is applied to calculate $p^-(n)$ for the negative ions:[43, 55]

$$p^-(n) = \frac{Z^-}{Z^0}\exp\left[\frac{-(\phi_{\mathrm{Au}} - E_{\mathrm{ea,Au}} - \delta_{\mathrm{ic}})}{k_{\mathrm{B}}T_{\mathrm{e}}(n)}\right] \tag{5.13}$$

where $E_{\mathrm{ea,Au}} = 2.308$ eV is the electron affinity of Au. By using Eqs. 5.5-5.10, 5.12 and 5.13, the relationship between the internal energy, charge and the yield of Au^- ion is shown in Figure 5.10 (b). For both positive and negative cases, the internal energy of the projectile after the impact should be the same. If we focus on the projectiles with -1 charge after the impact, the corresponding internal energy is ~500-550 eV, which is close to that of Au^+ ions (~450-500 eV). From the discussion on the positive ions above we know that due to the under-estimated ion yield, the internal energy is also under-estimated. In the calculations above, we didn't consider the evaporation of other Au clusters (Au_2 and Au_3) from the projectile. Considering the yield of Au_2^+ and Au_3^+ ion, 40% more Au in the negative mode and 70% more Au in the positive mode are evaporated from the Au projectile.

The power of the Au400 projectile cooling due to the radiation of photons has been calculated using the approach in [87]. Compared to the power of cluster cooling due to the evaporation of atoms, it is negligible in our experimental range of internal energies of the projectiles.

5.3.6 Coincidental detection of multi-charged projectiles and emitted $C_n^\pm$ ions

Again ~50% of the projectiles are ionized positively and negatively after impact (Figure 5.9 and discussion above). The experimental observation is that they are tied to the enhancement of emission of $C_n^\pm$ (Figure 5.7). This effect may be explained as follows.

71

The multi-charged projectile being aligned with the hole, induces the opposite charge at the surface area around the hole. The electric field lines between the projectile and the rim of the hole result in a dipole. The electric field of the dipole is strong due to the short distance and high charge. One can estimate the field of dipole at the surface of projectile as follows:

$$E_x = \frac{1}{4\varepsilon_0\pi}\frac{Q}{r_0^2} + \frac{x}{2\varepsilon_0}\int_{r_0}^{r_{\text{eff}}}\left[\frac{\beta(y)y}{(x^2+y^2)^{\frac{3}{2}}}\right]' \mathrm{d}y \tag{5.14}$$

where Q is the charge of nanoparticle, r_0 is the radius of nanoparticle and the primary hole in the graphene; $\beta(y)$ is the radial density of the charge around the primary hole; x is distance between the surface of nanoparticle and the hole plane. The boundary condition for the charge around the hole is $\int_{r_0}^{r_{\text{eff}}}\beta(y)\mathrm{d}y = Q$, where r_{eff} is the effective radius of the charge area around hole. Assuming that $r_{\text{eff}} \approx r_0$, the solution of the equation 5.14 for the field strength at the surface of the projectile is:

$$E_x = \frac{Q}{4\varepsilon_0\pi}\left(\frac{x}{(x^2+r_0^2)} + \frac{1}{r_0^2}\right) \tag{5.15}$$

The projectile experiences the charge exchange with the rim of hole at the distances less than the critical electron tunneling distance ($\sim$1 nm). Passing this short critical distance, the projectiles, which carry a multiple charge, are involved into the long distance dipole interaction. Thus, for $r_0 = 1$ nm, and $x = 1$ nm (critical distance), the strength of the field is 1 V/Å for $Q = 5$.

Due to the strong bonding of the poles of the dipole (field of $\sim$1 V/Å), the movement of the multi-charged projectile (one side of dipole) will bend and stretch the graphene around the hole. The projectile will experience an energy loss, when a part of projectile kinetic energy is transferred to the rim excitation due to the electrostatic interaction of the dipole poles. One should note that a graphene membrane

accumulates the strain energy very effectively due to its high Young's modulus ($\sim$1 TPa). The average energy loss of the projectile of $\sim$72 keV (Figure 5.2 and discussion above) is higher than the energy, which the projectile spends on the fast primary graphene rupturing and the carbon ejecta ($\sim$53 keV). We infer that part of the additional energy loss is due to the dipole projectile/hole rim interaction, and this energy is accumulated into the stretching of the graphene. One can consider the evolution of the stretched area as a surface solitary wave,[88] 26 which propagates toward the hole. The wave can focus strain energy of sufficient density around the hole to break C-C bonds, enlarge the hole size and stimulate abundant post-ejection of carbon clusters. The stripping of carbon ions due to the strong field of the dipole can be considered as an addition mechanism of the enlargement of the hole size.

Thus, the proposed effect of the nanoparticle-graphene dipole interaction may, at least partially, explain the experimental observations of a) high kinetic energy loss of the projectiles; b) enhancement of emission of $C_n^{\pm}$ when they co-detected with multi-charged projectiles; and c) large size of holes made by projectile impact, which are 8.9 ± 1.8 nm.[9]

5.4   Conclusion

The present study explores a projectile-target collision regime in-between macroscopic ballistic collisions and single atom-atom interactions. The key characteristics here are the high energy density developed in the interaction and the mode of dissipation into the graphene. Remarkably, the significant projectile energy loss cannot be fully accounted for with the size of the impact holes. The dissipation of the intense energy transient can in part be explained with a multi-charged projectile-graphene dipole interaction.

Another surprising observation is that 50% of the 520 keV Au_{400} are destroyed

in the collision with one graphene layer. The surviving projectiles carry an internal energy of $\sim$450-500 eV which is dissipated in a multi-fragmentation process resulting on average in the emission of $\sim$90-100 atoms. The internal energy is similar for projectiles with different charge states (positive, negative, or neutral) due to the equivalency of impacts on the homogeneous surface of the graphene.

Finally there is evidence of ample charge effects. The presence of negatively charged Au points to projectile neutralization prior to impact, and more importantly, is an indication of efficient simultaneous modes of positive and negative ionization of the projectiles. This observation suggests the possibility of detecting via transmission SIMS vanishingly small amounts of analyte deposited on graphene.

6. CHARACTERIZATION OF INDIVIDUAL FREE-STANDING NANOPARTICLES BY CLUSTER SIMS IN TRANSMISSION*

6.1   Introduction

The analysis of nanoparticles, NPs, with SIMS can be handled in one of two ways: analyzing an ensemble of NPs or testing them one by one. The latter enables to track changes in chemical reactivity with composition, a key issue when surface to volume ratios are large.[3] However extracting chemical information from a single vanishingly small object is very difficult to impossible. We side-step the limitation by probing a large number of NPs one-by-one and record the emissions from each NP separately. A large collection of NP will likely contain subsets of like-nanoparticles. Their data can be summed for statistics.[4] In this case, NPs must be dispersed to eliminate interaction among neighbors. Another concern is the contribution from the substrate. A solution is to deposit the NPs on graphene to reduce substrate contribution to the overall mass spectrum. Moreover, it then becomes feasible to run experiments in transmission, i.e., collecting the SIs in the forward direction, where emission is enhanced in comparison to the conventional backward emission.[18]

We present here a study of transmission SIMS for the analysis of NPs, specifically, 5 nm dodecanethiol-coated gold NPs deposited on graphene. We discuss below the characterization of graphene and of the NPs using $C_{60}^{1,2+}$ and Au_{400}^{4+} as projectiles at impact energies of ~ 0.42, 0.83 and 1.3 keV/atom respectively. The latter were chosen to maximize detection sensitivity, as they generate secondary ion yields which are two to three orders of magnitude larger than those from equal velocity atomic

---

ions.[7]

6.2 Experimental

6.2.1 Sample preparation

The graphene films used in this study were 3-5 layers (3-5L) free-standing graphene films on a lacey carbon net supported by a 300 mesh 3.05 mm standard copper TEM grid (Ted Pella, Inc., Redding, CA 96003). The coverage of graphene was typically 70-90% and this was verified by scanning electron microscopy (Figure 6.1). The grid was fixed on a 2 mm hole on a sample holder using silver print (MG Chemicals, Surrey, B.C., Canada V4N 4E7). The dodecanethiol-coated 5 nm gold nanoparticles (Nanoprobes, Yaphank, NY 11980) were suspended in hexane and diluted to 0.2 mg/mL. 1L of the solution was dropcast on the graphene film to form a sub-monolayer of Au NPs with a surface coverage of ∼50%. The Au NP has a 3-5 nm Au core (∼30,000 Au atoms) coated by a monolayer of ∼2 nm dodecanethiol. The TEM images of Au NPs (Figure 6.2) verified that the deposited Au NPs are self-assembled to form a sub-monolayer without agglomeration. Au NPs with the same concentration and volume were also dropcast on bulk pyrolytic graphite.

6.2.2 ToF-SIMS analysis

The experiments were run on a custom-built SIMS instrument with an effusive C_{60} source coupled to a linear time-of-flight mass spectrometer and a custom-built SIMS instrument with a Au-LMIS (liquid metal ion source) coupled to a linear time-of-flight, TOF, mass spectrometer. A detailed description can be found in Chapter 3. The samples were bombarded with individual 25 keV C_{60}^+, 50 keV C_{60}^{2+} and 520 keV Au_{400}^{4+} projectiles. The bombardment rate was adjusted to ∼1000 projectiles per second thus it was virtually impossible that multiple impacts hit the same site for 106 total impacts (less than 0.1% of the surface is analyzed). The projectile-graphene
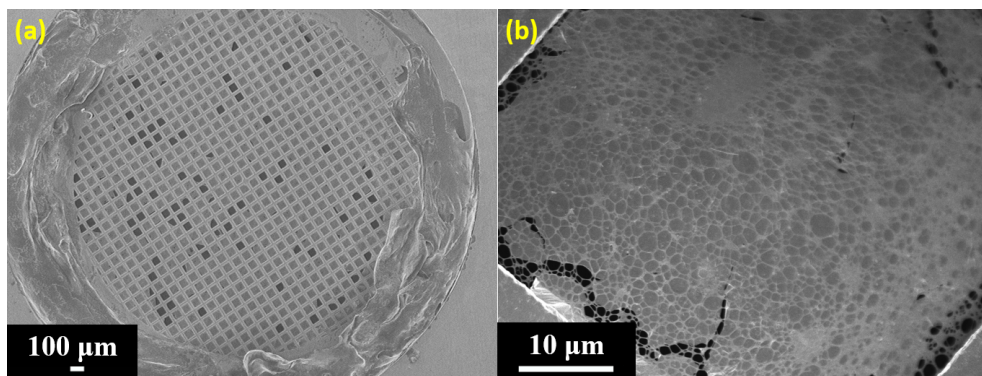
Figure 6.1: SEM images of the (a) graphene film on 3.05 mm Cu TEM grid fixed on a sample holder and (b) a square of TEM grid, showing the graphene film supported by lacey carbon net.
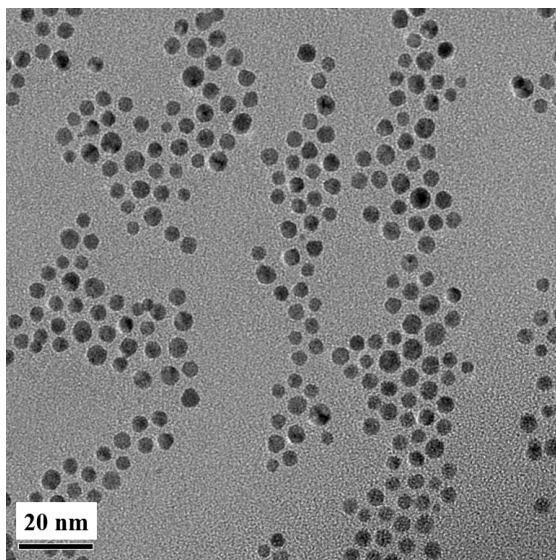
Figure 6.2: TEM image of the 5 nm dodecanethiol-coated Au NPs on 3-5L graphene.

bombardment angle was set at normal. The impact angle is critical for recovering a maximum of SIs. The SIs and secondary electrons, SEs, from each individual impact was detected separately in the transmission direction by using the "event-by-event bombardment/detection mode".[35] The data were recorded and processed using custom-designed software.[41] By selecting a specific ion of interest in the total mass spectrum, the co-emitted and therefore co-localized ions were extracted, resulting in a coincidence ion mass spectrum.[4] From the coincidence ion mass spectrum one can calculate the effective yield (Y_e), which is determined as follows: [22]

$$Y_{e,A} = \frac{I_{A,B}}{I_B} \tag{6.1}$$

where $Y_{e,A}$ is the effective yield of ion A. $I_{A,B}$ is the intensity of ion A in the coincidence ion mass spectrum with ion B, and I_B is the intensity of ion B in the total mass spectrum. Y_e is the number of a specified SI emitted per projectile impact on the NP, excluding impacts on the substrate. Y_e also accounts for differences in NP coverage among samples.

6.3   Results and discussion

6.3.1   Characterization of graphene

The 3-5 layer graphene was bombarded with 25 keV C_{60}^+ and 50 keV C_{60}^{2+} projectiles in the transmission mode (spectra shown in Figure 6.3). The C_n^- carbon clusters ranging from C^- to C_{10}^- followed by C_nH^- and $C_nH_2^-$ are the main features of this spectra. Beyond m/z 120, the contribution from graphene becomes negligible, an advantageous feature for characterizing functionalized NPs. The first carbon peak C^- has a distinct tail shape in the spectra obtained with C_{60} projectiles at 25 and 50 keV respectively. This feature does not appear on large carbon cluster peaks. The initial kinetic energy distribution of C^- extends up to 1/60 of the kinetic energy of

the incident projectiles: 0.42 keV for 25 keV C_{60}^+ and 0.83 keV for 50 keV C_{60}^{2+}, which is contributed by the knocked-on carbon atoms from the graphene and the shattered carbon atoms from the projectiles.[43]

6.3.2 Characterization of gold nanoparticles

The negative spectra of Au NPs on graphene bombarded with 50 keV C_{60}^{2+} are presented in Figure 6.4 In spectrum (a) C_{60}^{2+} bombarded the graphene film first, then the Au NPs, while in spectrum (b), C_{60}^{2+} bombard Au NPs first, then the graphene film. It must be noted that the graphene film is supported by a lacey carbon net, which has a thickness of $\sim$100 nm.[42] Thus in the transmission direction no start signal can be obtained from the lacey carbon net or Cu grid. Thus virtually all signals are from impacts on graphene. In both spectra the peaks of Au-, Au adduct ions and the oxidized molecular ion ($C_{12}H_{25}SO_3^-$, m/z 249) from the layer of dodecanethiol were observed. The mass resolution of the Au- peak is about 350. The effective yields of Au are similar in both cases ($Y_e = 1.7\%$ and 1.8% respectively). All effective yields are measured in the coincidence mass spectra with SH^-, which is a characteristic peak of the Au NPs. However, the effective yield of the molecular ion peak in (b) is lower than that in (a) ($Y_e = 0.15\%$ and 0.62% respectively). We attribute the lower yield in case (b) to the emission of the molecular moiety being blocked by the graphene film, while single Au atomic ions and small Au adducts are able to penetrate through the graphene film. However, when the projectiles impact on graphene first, there is no hindrance to the SI emission. Therefore, the effective yield of the oxidized molecular ion of dodecanethiol enables to determine on which side of the graphene the Au NPs are deposited.

The difference in the data obtained from the NPs in transmission versus from the same NPs deposited on a thick substrate is illustrated in Figure 6.5 Spectrum (a)
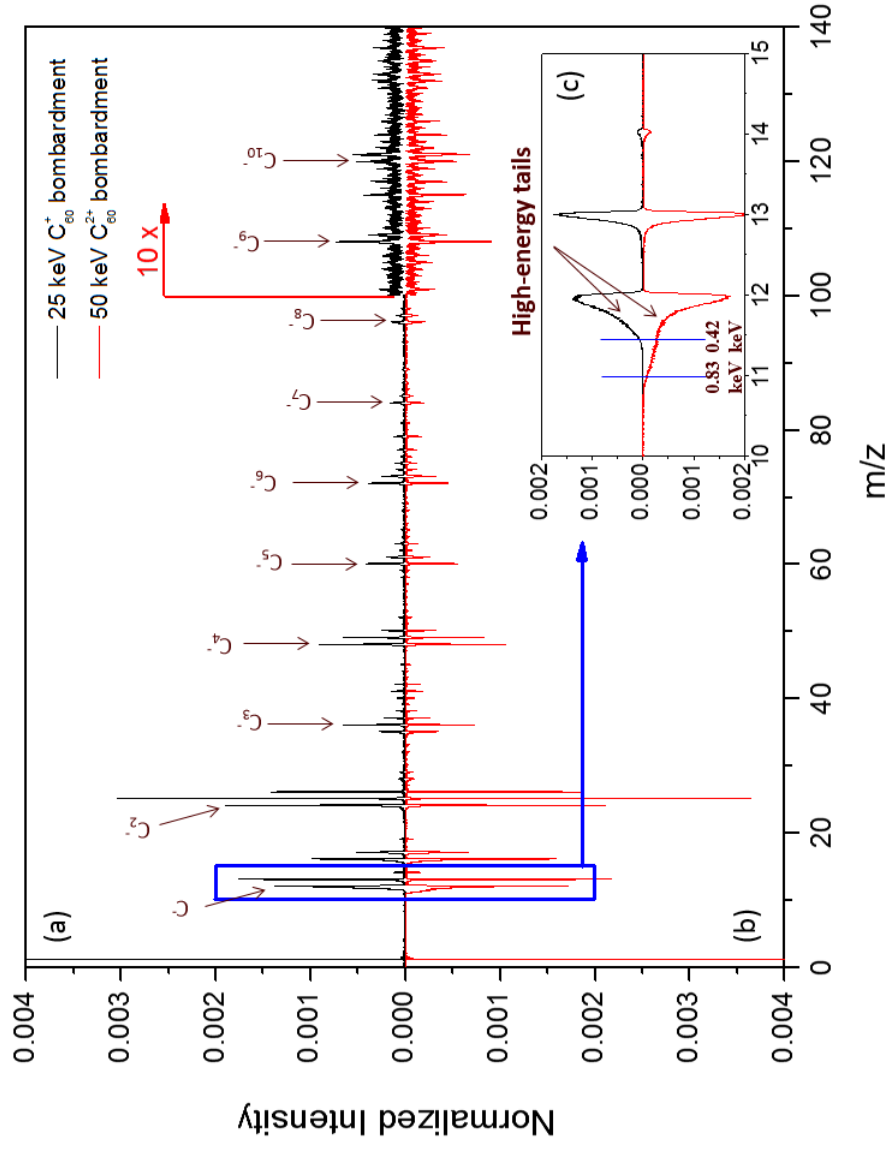
Figure 6.3: Negative mass spectra of the 3-5L graphene in transmission bombarded with (a) 25 keV C_{60}^+, (b) 50 keV C_{60}^{2+} and (c) details of the high-energy tails of C^- peaks (peak height is normalized to total events).
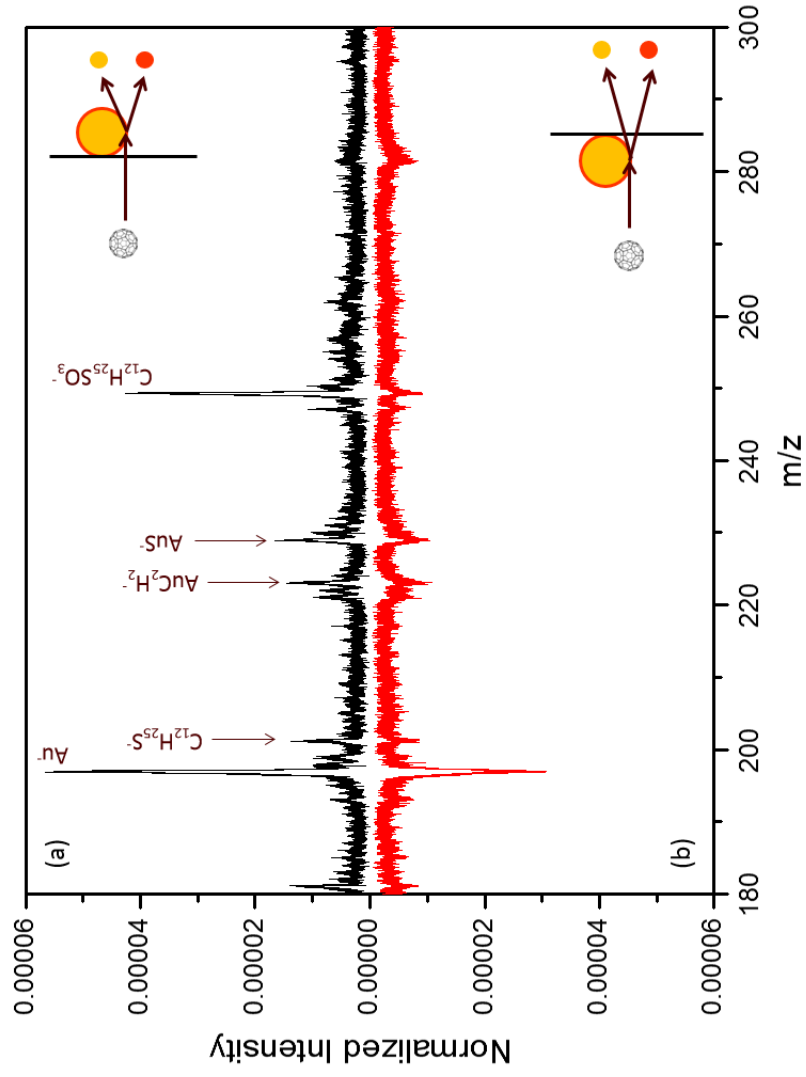
Figure 6.4: Negative mass spectra of the 5 nm Au NPs deposited on 3-5L graphene in transmission bombarded with 50 keV C_{60}^{2+}. (a) Graphene was bombarded first; (b) Au NPs were bombarded first (peak height is normalized by the number of projectile impacts).

is from a sub-monolayer of Au NPs deposited on bulk pyrolytic graphite substrate. The SIs were obtained in the conventional reflection direction. Spectrum (b) is from Au NPs on 3-5L graphene bombarded with C_{60}^{2+}. The surface coverage of Au NPs on substrates was similar in both cases ($\sim$30%). It should be noted that the effective yield of $C_{12}H_{25}SO_3^-$ is $\sim$4 times higher in the transmission mode than that in the reflection mode ($Y_e = 0.62\%$ vs. 0.16%). In the reflection mode, most of the SIs are from direct impacts of C_{60}^{2+} on Au NPs, which leads to a higher yield of Au atomic ions ($Y_e = 4.2\%$ in the reflection mode and 1.7% in the transmission mode) and Au adducts in the reflection direction. Given the thick substrate, the ejecta result from a high density collision cascade.[89] In the transmission mode, the SIs are from grazing impacts, favoring the emission of fragments and molecular ions from the dodecanethiol layer. However overlapping collision cascades cannot develop in graphene, yet the effective yield of the molecular ion is higher in the transmission mode. The possible mechanism(s) are discussed below. The comparison shows that transmission SIMS is more suitable for the characterization of molecular ions attached to NPs than conventional reflection SIMS.

A comparison of the spectra obtained with different projectiles is shown in Figure 6.6 Spectrum (a) is from 520 keV Au_{400}^{4+} bombardment and spectrum (b) is from 50 keV C_{60}^{2+} bombardment. The two spectra contain similar peaks: Au^-, Au^{2-} (not shown), Au adduct ions and the ions from dodecanethiol ($C_{12}H_{25}S^-$, $C_{12}H_{25}SO_3^-$, $C_{12}H_{25}SO_4^-$, etc.). It should be noted that the y-axis scales on the two spectra are different. The yields of SIs from Au_{400}^{4+} bombardment are $\sim$3 times higher than the yields of the same SIs from C_{60}^{2+} bombardment. For instance, the dodecanethiol molecular ion peak at m/z 249 has a Y_e of 2.0% from Au_{400}^{4+} bombardment and a Y_e of 0.62% from C_{60}^{2+} bombardment. The high Y_e of Au^- from Au_{400}^{4+} bombardment compared to that from C_{60}^{2+} bombardment (10.0% vs. 1.7%) is because part of the

82

Figure 6.5: Negative mass spectra of the 5 nm Au NPs deposited on (a) bulk pyrolytic graphite measured in the reflection mode and (b) 3-5L graphene measured in the transmission mode, bombarded with 50 keV C_{60}^{2+} (peak height is normalized by the number of projectile impacts).

83
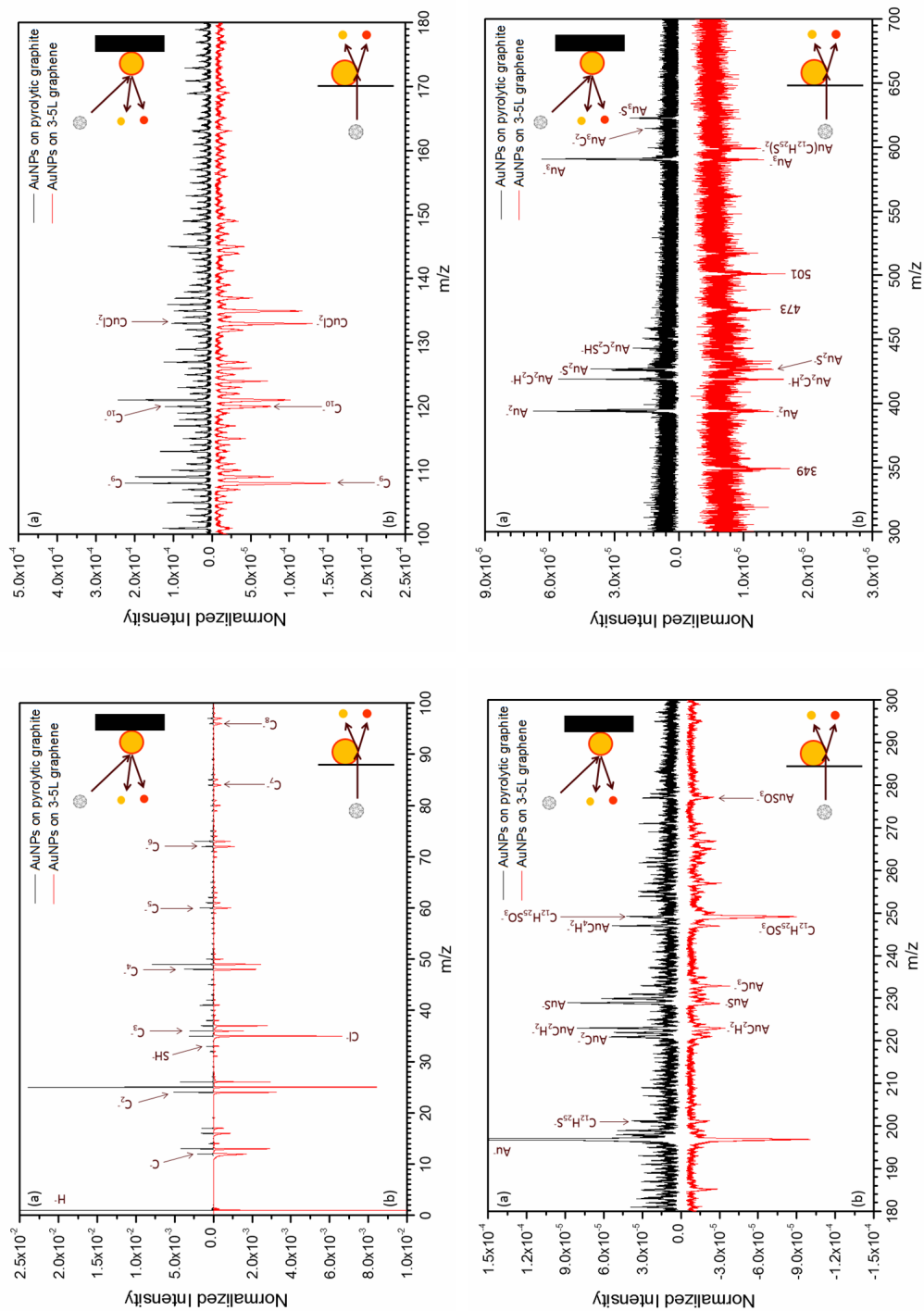
Table 6.1: Effective yields of Au^- and $C_{12}H_{25}SO_3^-$ of Au NPs coincidental with SH^-.

	C_{60}^{2+} bombardment			Au_{400}^{4+} bombardment
	GF^a, T^b	NPF^c, T	Graphite, R^d	GF, T
Au^-	1.7%	1.8%	4.2%	10.0%
$C_{12}H_{25}SO_3^-$	0.62%	0.15%	0.16%	2.0%

^{a}The projectiles impact the graphene first (GF), then the Au NPs.
^{b}In the transmission mode.
^{c}The projectiles impact nanoparticles first (NPF), then the graphene.
^{d}In the reflection mode.

Au^- is from the Au_{400}^{4+} projectiles. The comparison of the effective yields for all cases discussed above are listed in Table 6.1.

A question that arises is that of the mechanism(s) of ejecta emission and ionization, given that the dimensions of the NPs are not sufficient for complete projectile energy deposition.[34] The SIs originate either from the support, the Au NP or its self-assembled layer of dodecanethiol. During the impact of C_{60}^{2+} on graphene, the projectile is shattered and atomized via atom-atom collisions. The ejected carbon atoms from the projectile and knocked-on carbon atoms from graphene then interact with the Au NPs in the transmission direction.[43] In contrast, when Au_{400}^{4+} impacts on graphene, the projectile is not shattered but penetrates through graphene and interacts with the AuNPs.[9] The Au-Au collision is more efficient for kinetic energy transfer than a C-Au collision. The projectile impact parameter plays a role[43]: in the case of C_{60}^{2+} bombardment, the SI signals are from grazing impacts, while in the case of Au_{400}^{4+} bombardment, the SI signals can be obtained from both grazing and direct impacts on the Au NPs.
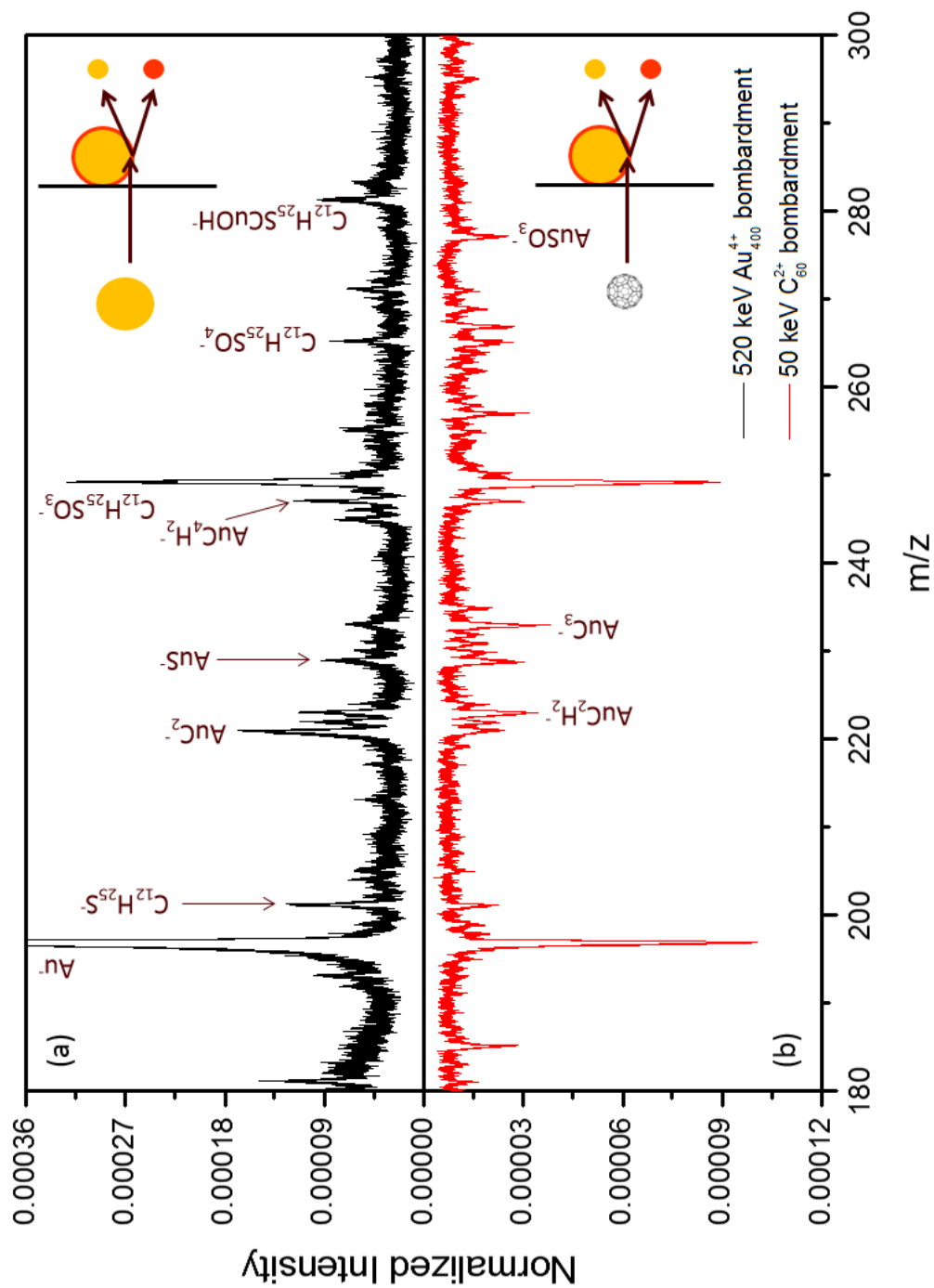
Figure 6.6: Negative mass spectra of the 5 nm Au NPs deposited on 3-5L graphene in transmission bombarded with (a) 50 keV C_{60}^{2+} and (b) 520 keV Au_{400}^{4+} (peak height is normalized by the number of projectile impacts).

6.4 Conclusion

We present a characterization of the graphene film alone and the Au NPs deposited on graphene substrate. Graphene is a promising ultra-thin substrate for the analysis of NPs in transmission SIMS since it doesnt interfere with peaks from the NPs above m/z 120. Transmission SIMS readily indicates on which side of the graphene film the analyte is deposited. Compared to conventional reflection SIMS on bulk support, transmission SIMS provides $\sim$4 times higher yield for the molecular ion attached to 5 nm NPs. Comparing projectiles in transmission, the yields for the molecular moiety are $\sim$3 times higher in Au_{400}^{4+} bombardment at 1.3 keV/atom than C_{60}^{2+} bombardment at 0.83 keV/atom. It is important to recall that the respective mechanisms of projectile-graphene/NP interactions are fundamentally different.[43, 9] A final caveat for reproducible transmissions experiments is the requirement of a well-defined projectile-target geometry.

7. CONCLUSION

7.1 Massive cluster-2D material interaction

From the study we have learnt that the projectile-graphene interaction is fundamentally different from the projectile-3D material interaction. The key characteriztics are a surprisingly high projectile kinetic energy loss during the impact, a multi-step fragmentation of the excited projectile after the impact, and neutralization and re-ionization (positively and negatively) in the process. Moreover, abundant SI emission was observed in the transmission direction. Based on the experimental data, two distinct mechanisms of projectile-target interactions are proposed for C_{60} and Au_{400} respectively. They should be validated with experiments at lower and higher impact energies and on other 2D targets than graphene, such as graphane, silicene, germanene, molybdenum disulfide, boron nitride, etc. All of those have different chemical, electronic and mechanical properties than graphene, facilitating different applications of nano-object characterization. For example, boron nitride is a suitable substrate for Au and Ag nanoparticle deposition.[90, 91]

Future investigations should again focus on the fate of the projectile, the SI yield, and the energetics of the interaction. The energy loss and projectile survival/fragmentation can be studied by varing the target thickness. For instance, stacked graphene films can be used such that the intact/fragmented projectiles after passing through the first graphene film will further impact the second one. Small increase in graphene thickness can be obtained by rotating the target with respective to the incident projectile. The SI emission in both the transmission and reflection directions from the cases noted above have been reported,[7, 8, 9] but the fate of the projectiles and the energetics of the interaction have yet to be studied. MD sim-

ulations help understand the interactions, based on the emission of neutral ejecta, the evolution of the projectile and the impact hole on graphene. In chapter 4 some results of the MD simulation of the C_{60} impact on graphene are shown. The current limitation of MD simulation appear clearly in the case of massive Au gluster impact on graphene. For instance, the holes predicted[47] are 2-3 times smaller than those observed experimentally[9]. Indeed the MD simulation cannot account for the projectile-graphene dipole interaction proposed in Chapter 5.

7.2 Characterization of nanoparticles

The present work shows the potential of using graphene films as the substrate for analyzing individual NPs. Enhanced molecular ion yields are obtained in the transmission direction ($4\times$ higher SI yield for the molecular ion of the dodecanethiol coating of the AuNPs compared to that in the reflection direction). The projectiles also play a role here: Au_{400}^{4+} 91.3 keV/atom) is $3\times$ more efficient than C_{60}^{2+} (0.83 keV/atom) when producing molecular ions, due to more efficient energy transfer between the Au projectiles and the AuNPs.

The limit of detections (defined as 3 times of the standard deviation of the background) with C_{60}^{2+} and Au_{400}^{4+} impact for the surface ligand (dodecanethiol) are 1.6 pg and 5.2×10^2 fg respectively.[92]

7.3 Future work

The aim of future work should be to validate transmission SIMS for semi-quantitative analysis, and to improve the detection sensitivity of transmission SIMS. The issues to be addressed are outlined below.

7.3.1   Sample preparation

Deposition of analytes on graphene film is a challenge and critical for the transmission SIMS experiment. Some NPs may agglomerate on graphene due to their high hydrophilicity, which reduces the surface coverage (therefore the number of effective impacts) and more importantly, prevents the projectiles from passing through the target. To solve this problem, oxidized graphene films could be used. The functional groups containing H and O such as -OH and -COOH provide a higher hydrophilicity of the graphene surface, which improves the deposition of the NPs with hydrophilic coatings and/or in the aqueous solutions. For more specific requirements, the graphene surface can be functionalized to introduce functional group(s)[93] that help anchor the NPs with the matching functional groups in the coating molecules. The "coffee-stain" effect is another problem leading to an inhomogeneity layer when depositing nanoparticles by drop-casting . This problem can be overcome by drying the aqueous droplet in an ethanol vapor atmosphere.[94]

The drop-casting technique is limited to the solubility and the hydrophilicity of the analyte. Another method for depositing a thin film on the target is chemical vapor deposition (CVD). Typically in the Schweikert lab the thickness of the CVD layer is in the order of several hundred nanometers. In order to make single-layer deposition for transmission-SIMS experiments, a shutter (with the exposure time 1/10 s or less) set between the CVD source (the oven) and the target is required. This allows to deposit as little as a few attomoles of analyte.

7.3.2   Enhancement of the mass resolution

In our experiments, one of the limitation of the mass resolution is the length of the ToF-MS. For example, in the Au_{400}-SIMS instrument (Chapters 5, 6), the length of the linear ToF-MS in the transmission direction is 66 cm and the mass resolution

(defined as the mass divided by the peak width at FWHM) for the $C_{12}H_{25}SO_3^-$ peak at m/z 249 is 480. The mass resolution can be improved with a longer flight path using a reflectron ToF-MS. For instance, a resolution of ~1600 at m/z 26 can be achieved with a reflectron with a total length of 176 cm.[40]

7.3.3   Enhancement of the transmission efficiency

As noted in Chapter 5, the transmission/detection efficiency for the Au_{400}-SIMS in the transmission direction is ~0.4. This parameter can be improved with precision alignment of the projectile-target trajectory. Indeed if the incident projectile is not perpendicular to the target surface, it and exiting fragments will carry additional radial momenta. Some of them will be outside the angle of acceptance of the detector. A well-defined projectile-target geometry is also critical for experiments focusing on the fate of the projectiles because the projectile and the fragments exiting the target have an additional radial momentum if the incident projectile is not perpendicular to the target.

7.3.4   Size-dependent SI emission

In summary, for NPs with diameters of 2-50 nm, the SIs emitted per impact depend on the impact parameter, e.g. a direct or a grazing impact.[61, 34] For the smaller Au NPs (Au_{55}, Au_{147} and Au_{225}), a linear increase of the yield of Au_2CN^- with the increase of the number of Au atoms was reported,[95] i.e. all impacts are equivalent. However, there are no relevant data yet in transmission. One may expect again that all impacts are equivalent from NPs smaller than 2 nm. For larger NPs, there should be a pronounced dependence on the impact parameter.

7.3.5 Size and energy of the projectile

In order to improve the detection sensitivity, larger and more energetic projectiles may be used, because the SI yield increases with the increase of the number of atoms in the cluster projectile and the kinetic energy (velocity) of the projectile (see the discussion in Chapters 1, 2 and 4). To increase the kinetic energy of the Au projectiles, a platform at a higher voltage (> 100 kV for the Au-LMIS in Schweikert lab) is needed. For instance, the yield of the glycine molecular ion increases by one order of magnitude as the impact energy of Au_{400}^{4+} increases from 100 keV/q to 4 Mev/q.[36] More massive cluster projectiles (e.g. Au_{3000}^{8+}) hold promise for single impact SIMS due to the high SI multiplicity, resulting in a higher detection sensitivity, and more information about the co-localized SIs. For instance, Number of emitted SIs per impact increases from 12 to 31 when the size of the Au_n^{q+} projectiles increase from n/q 100 to 350, at an impact energy of $130q$ keV.[96]

7.3.6 New projectiles

Another option for increasing the SI yields is to consider other projectiles. For instance Bi_{100q}^{q+} has been shown in preliminary experiments at IPNO to carry a higher charge state than a similar size Au_{100q}^{q+}. Another way may be to embed monodisperse NPs in an ionic conductor such as polyethylene glycol, PEG, in lieu of the Au-Si eutectic solid in the LMIS. The LMIS then becomes an "Ionic Liquid Particle Source". Alternatively, NPs dissolved in ionic liquids can also be electrosprayed,[97] and the LMIS could be relplaced with an ESI set-up.

REFERENCES

[1] J. Shang and X. Gao. *Chem. Soc. Rev.*, 43:7267, 2014.

[2] D. V. Talapin and E. V. Shevchenko. *Chem. Rev.*, 116:10343, 2016.

[3] S. C. S. Lai, P. V. Dudin, J. V. Macpherson, , and P. R. Unwin. *J. Am. Chem. Soc.*, 133:10744, 2011.

[4] M. A. Park, K. A. Gibson, L. Quinones, and E. A. Schweikert. *Anal. Chem.*, 248:988, 1990.

[5] M. J. Van Stipdonk, R. D. Harris, and E. A. Schweikert. *Rapid Commun. Mass Spectrom.*, 10:1987, 1996.

[6] J. D. DeBord, F. A. Fernandez-Lima, S. V. Verkhoturov, E. A. Schweikert, and S. Della-Negra. *Surf. Interface Anal.*, 45:134, 2013.

[7] J. D. DeBord, S. Della-Negra, F. A. Fernandez-Lima, S. V. Verkhoturov, and E. A. Schweikert. *J. Phys. Chem. C*, 116:8138, 2012.

[8] J. D. DeBord. PhD Thesis, Texas A & M University, 2012.

[9] M. J. Eller, C.-K. Liang, S. Della-Negra, A. B. Clubb, H. Kim, A. E. Young, and E. A. Schweikert. *J. Chem. Phys.*, 142:044308–1, 2015.

[10] A. Benninghoven. *Phys. Status Solidi B*, 34:K169, 1969.

[11] S. Lozano-Perez, M. Schröder, T. Yamada, T. Terachi, C.A. English, and C.R.M. Grovenor. *Appl. Surf. Sci.*, 255:1541, 2008.

[12] A. D. Appelhans and J. E. Delmore. *Anal. Chem.*, 91:1087, 1989.

[13] M. G. Blain, S. Della-Negra, H. Joret, Y. Le Beyec, and E. A. Schweikert. *Phys. Rev. Lett.*, 63:1625, 1989.

[14] S. Bouneau, A. Brunelle, S. Della-Negra, J. Depauw, D. Jacquet, Y. Le Beyec, M. Pautrat, M. Fallavier, J. C. Poizat, and H. H. Andersen. *Phys. Rev. B*, 65:144106, 2002.

[15] N. Winograd. *Anal. Chem.*, 77:142A, 2005.

[16] A. Tempez, J. A. Schultz, S. Della-Negra, J. Dephaw, D. Jacquet, A. Novikov, Y. Le Beyec, M. Pautrat, M. Caroff, M. Ugarov, H. Bensaula, M. Gonin, K. Fuhrer, and A. Woods. *Rapid Commun. Mass Spectrom.*, 18:371, 2004.

[17] C.-K. Liang. PhD Thesis, Texas A & M University, 2014.

[18] Y. Huang, J. Wu, and K. Hwang. *Phys. Rev. B*, 74:245413, 2006.

[19] C. Carpenter, D. Maroudas, and A. Ramasubramaniam. *Appl. Phys. Lett.*, 103:013102, 2013.

[20] L. Liu, J. Zhang, J. Zhao, and F. Liu. *Nanoscale*, 4:5910, 2012.

[21] M. J. Eller, S. V. Verkhoturov, S. Della-Negra, R. D. Rickman, and E. A. Schweikert. *Surf. Interface Anal.*, 43:484, 2011.

[22] M. J. Eller, S. V. Verkhoturov, S. Della-Negra, and E. A. Schweikert. *J. Phys. Chem. C*, 84:103706–1, 2013.

[23] W. D. Davis. *J. Vac. Sci. Technol.*, 10:278, 1973.

[24] P. J. McKeown, M. V. Johnston, and D. M. Murphy. *Anal. Chem.*, 63:2069, 1991.

[25] D. A. Lake, M. P. Tolocka, M. V. Johnston, and A. S. Wexler. *Environ. Sci. Technol.*, 37:3268, 2003.

[26] Y. X. Su, M. F. Sipin, H. Furutani, and K. A. Prather. *Anal. Chem.*, 76:712, 2004.

[27] A. Zelenyuk, Y. Cai, L. Chieffo, and D. Imre. *Aerosol Sci. Technol.*, 39:554, 2005.

[28] S. Y. Wang and M. V. Johnston. *Int. J. Mass Spectrom.*, 258:50, 2006.

[29] S. Y. Wang; C. A. Zordan; M. V. Johnston. *Anal. Chem.*, 78:1750, 2006.

[30] V. Pinnick, S. V. Verkhoturov, L. Kaledin, and E. A. Schweikert. *Anal. Chem.*, 80:9052, 2008.

[31] S. Rajagopalachary, S. V. Verkhoturov, and E. A. Schweikert. *Anal. Chem.*, 81:1089, 2009.

[32] L.-J. Chen, S. S. Shah, J. Silangcruz, M. J. Eller, S. V. Verkhoturov, A. Revzin, and E. A. Schweikert. *Int. J. Mass. Spectrom.*, 303:97, 2011.

[33] M. J. Eller, S. V. Verkhoturov, S. Della-Negra, and E. A. Schweikert. *J. Phys. Chem. C*, 114:17191, 2010.

[34] C.-K. Liang, S. V. Verkhoturov, L.-J. Chen, and E. A. Schweikert. *Int. J. Mass. Spectrom*, 334:43, 2013.

[35] S. V. Verkhoturov, M. J. Eller, R. D. Rickman, S. Della-Negra, and E. A. Schweikert. *J. Phys. Chem. C*, 114:5637, 2010.

[36] S. Della-Negra, J. Arianer, J. Depauw, S. V. Verkhoturov, and E. A. Schweikert. *Surf. Interface Anal.*, 43:66, 2011.

[37] S. Bouneau, S. Della-Negra, J. Depauw, D. Jacquet, Y. Le Beyec, J. P. Mouffron, A. Novikov, and M. Pautrat. *Nucl. Instrum. Methods Phys. Res., Sect. B*, 225:579, 2004.

[38] J. L. Wiza. *Nucl. Instrum. Methods*, 162:587, 1979.

[39] R. D. Rickman, S. V. Verkhoturov, G. J. Hager, E. A. Schweikert, and J. A. Bennett. *Int. J. Mass Spectrom.*, 241:57, 2005.

[40] M. J. Eller. PhD Thesis, Texas A & M University, 2012.

[41] L.-J. Chen, J. H. Seo, M. J. Eller, S. V. Verkhoturov, S. S. Shah, A. Revzin, and E. A. Schweikert. *Anal. Chem.*, 83:7173, 2011.

[42] G. Karlsson. *J. Microsc.*, 203:326, 2001.

[43] S. V. Verkhoturov, S. Geng, B. Czerwinski, A. E. Young, A. Delcorte, and E. A. Schweikert. *J. Chem. Phys.*, 143:164302–1, 2015.

[44] S. V. Verkhoturov, R. D. Rickman, C. Guillermier, G. J .Hager, J. E. Locklear, and E. A. Schweikert. *Appl. Surf. Sci.*, 252:6490, 2006.

[45] R. D. Harris, W. S. Baker, M. J. Van Stipdonk, R. M .Crooks, and E. A. Schweikert. *Rapid Commun. Mass Spectrom.*, 13:1374, 1999.

[46] R. Behrisch and W. Eckstein. *Sputtering by Particle Bombardment: Experiments and Computer Calculations from Threshold to MeV Energies*. Springer-Verlag, 2007.

[47] S. Zhao, J. Xue, L. Liang, Y. Wang, and S. Yan. *J. Phys. Chem. C*, 116:11776, 2012.

[48] A. D. Bekkerman, N. Kh. Dzhemilev, S. E. Maksimov, V. V. Solomko, S. V. Verkhoturov, and I. V. Veryovkin. *Vacuum*, 47:1073, 1996.

[49] J. D. Watts and R. J. Bartlett. *J. Chem. Phys*, 97:3445, 1992.

[50] B. J. Garrison and Z. Postawa. *Mass Spectrom. Rev.*, 27:289, 2008.

[51] S. J. Stuart, A. B. Tutein, and J. A. Harrison. *J. Chem. Phys*, 112:6472, 2000.

[52] B. Czerwinski and A. Delcorte. *Surf. Interface Anal.*, 46:11, 2014.

[53] B. M. Smirnov. *Phys.-Usp.*, 44:221, 2001.

[54] M. L. Yu and N. D. Lang. *Nucl. Instrum. Methods Phys. Res., Sect. B*, B14:403, 1986.

[55] Z. Sroubek, X. Chen, and J. A. Yarmoff. *Phys. Rev. B*, 73:045427, 2006.

[56] J. D. DeBord, S. V. Verkhoturov, L. M .Perez, S. W. North, M. B. Hall, and E. A. Schweikert. *J. Chem. Phys*, 138:214301–1, 2013.

[57] S. Cernusca, H. P. Winter, F. Aumayr, R. Diez Muino, and J. I. Juaristi. *Nucl. Instrum. Methods Phys. Res., Sect. B*, 203:1, 2003.

[58] H. S. W. Massey. *Negative Ions.* MgGraw-Hill Int. Book Co., 1982.

[59] B. Baguenard, J. C. Pinare, F. Lepine, C. Bordas, and M. Broyer. *Chem. Phys. Lett*, 352:147, 2002.

[60] R. Zan, Q. M. Ramasse, U. Bangert, and K. S. Novoselov. *Nano Lett.*, 12:3936, 2012.

[61] S. Rajagopalachary, S. V. Verkhoturov, and E. A. Schweikert. *Nano Lett.*, 8:1076, 2008.

[62] C.-K. Liang, M. J. Eller, S. V. Verkhoturov, and E. A. Schweikert. *J. Am. Soc. Mass Spectrom.*, 26:1259, 2015.

[63] B. I. Costescu and F. Gräter. *Phys. Chem. Chem. Phys.*, 16:12582, 2014.

[64] S. Liu, Q. Zhao, J. Xu, K. Yan, H. Peng, F. Yang, L. You, and D. Yu. *Nanotechnology*, 23:085301, 2012.

[65] S. Garaj, W. Hubbard, A. Reina, J. Kong, D. Branton, and J. A. Golovchenko. *Nature*, 467:190, 2010.

[66] G. Hu, M. Mao, and S. Ghosal. *Nanotechnology*, 23:395501, 2012.

[67] G. F. Schneider, Q. Xu, S. Hage, S. Luik, J. N. H. Spoor, H. Zandbergen S. Malladi, and C. Dekker. *Nat. Commun.*, 4:2619, 2013.

[68] G. Ganteför and W. Eberhardt. *Phys. Rev. Lett.*, 77:4524, 2008.

[69] R. D. Rickman, S. V. Verkhoturov, E. S. Parilis, and E. A. Schweikert. *Phys. Rev. Lett.*, 92:047601–1, 2004.

[70] S. Bouneau, S. Della-Negra, J. Depauw, D. Jacquet, Y. Le Beyec, J. P. Mouffron, A. Novikov, and M. Pautrat. *Nucl. Instru. Meth. B*, 225:579, 2004.

[71] J. T. Miller, A. J. Kropf, Y. Zha, J. R. Regalbuto, L. Delannoy, C. Louis, E. Bus, and J. A. van Bokhoven. *J. Catal.*, 240:222, 2006.

[72] J. F. Ziegler, J. P. Biersack, and U. Littmark. *The Stopping and Range of Ions in Solids.* Pergamon, 1985.

[73] P. W. Geno and R.D. Macfarlane. *Int. J. Mass Spectrom.*, 92:195, 1989.

[74] J. Riordan. *An Introduction to Combinatorial Analysis.* John Wiley & Sons, 1958.

[75] C. E. Klots. *Z. Phys. D.*, 5:83, 1987.

[76] C. E. Klots. *J. Phys. Chem.*, 92:5864, 1988.

[77] C. Bréchignac, P. Cahuzac, J. Leygnier, and J. Weiner. *J. Chem. Phys.*, 90:1492, 1989.

[78] H. Haberland. *Clusters of Atoms and Molecules. Theory, Experiment, and Clusters of Atoms.* Springer-Verlag, 1994.

[79] B. M. Smirnov. *Phys.-Usp.*, 36:933, 1993.

[80] H. Haberland. *Clusters of Atoms and Molecules. Theory, Experiment, and Clusters of Atoms.* Springer-Verlag, 1994.

[81] R. S. Berry and B. M. Smirnov. *Phys. Rep.*, 527:205, 2013.

[82] W. M. Haynes. *CRC Handbook of Chemistry and Physics, 96th Edition.* CRC Press, 2015.

[83] J. Cetnar. *Ann. Nucl. Energy*, 33:640, 2006.

[84] D. M. Wood. *Phys. Rev. Lett.*, 46:749, 1981.

[85] C. Bréchignac, P. Cahuzac, F. Carlier, and J. Leygnier. *Phys. Rev. Lett.*, 63:1368, 1989.

[86] E. Gruber, R. A. Wilhelm, R. Pétuya, V. Smejkal, R. Kozubek, A. Hierzenberger, B. C. Bayer, I. Aldazabal, A. K. Kazansky, F. Libisch, A. V. Krasheninnikov, M. Schleberger, S. Facsko, A. G. Borisov, A. Arnau, and F. Aumayr. *Nat. Commun.*, 7:13948, 2016.

[87] B. M. Smirnov. *Cluster Processes in Gases and Plasmas.* Wiley-VCH Verlag GmbH & Co. KGaA, 2010.

[88] M. Fujimoto. *Introduction to the Mathematical Physics of Nonlinear Waves.* Morgan & Claypool, 2014.

[89] P. Sigmund. *Nucl. Instrum. Methods Phys. Res., Sect. B*, 27:1, 1987.

[90] S. K. Singhal, V. Kumar, K. Stalin, A. Choudhary, S. Teotia, G. B. Reddy, R. B. Mathur, S. P. Singh, and R. Pasricha. *Part. Part. Sys. Char.*, 30:445, 2013.

[91] F. Wang, X. Zeng, Y. Yao, R. Sun, J. Xu, and C.-P. Wong. *Sci. Rep.*, 6:19394, 2016.

[92] H. Hinterwirth, S. Kappel, T. Waitz, T. Prohaska, W. Lindner, and M. Lämmerhofer. *ACS Nano*, 7:1129, 2013.

[93] V. Biju. *Chem. Soc. Rev.*, 43:744, 2014.

[94] M. Majumder, C. S. Rendall, J. A. Eukel, J. Y. L. Wang, N. Behabtu, C. L. Pint, T.-Y. Liu, A. W. Orbaek, F. Mirri, J. Nam, A. R. Barron, R. H. Hauge, H. K. Schmidt, and M. Pasquali. *J. Phys. Chem. B*, 116:6536, 2012.

[95] A. B. Clubb, M. J. Eller, S. V. Verkhoturov, E. A. Schweikert, R. M. Anderson, and R. M. Crooks. *J. Vac. Sci. Technol. B*, 34:03H104–1, 2016.

[96] Personal communication with A. Vinjamuri and M. J. Eller.

[97] D. Grafahrend, P. Jungbecker, G. Seide, H. Leonards, T. Gries, M. Möller, and D. Klee. *The Open Chemical and Biomedical Methods Journal*, 3:1, 2010.